Cancer Cell

Article

EGFR-activated myofibroblasts promote metastasis of pancreatic cancer

Graphical abstract

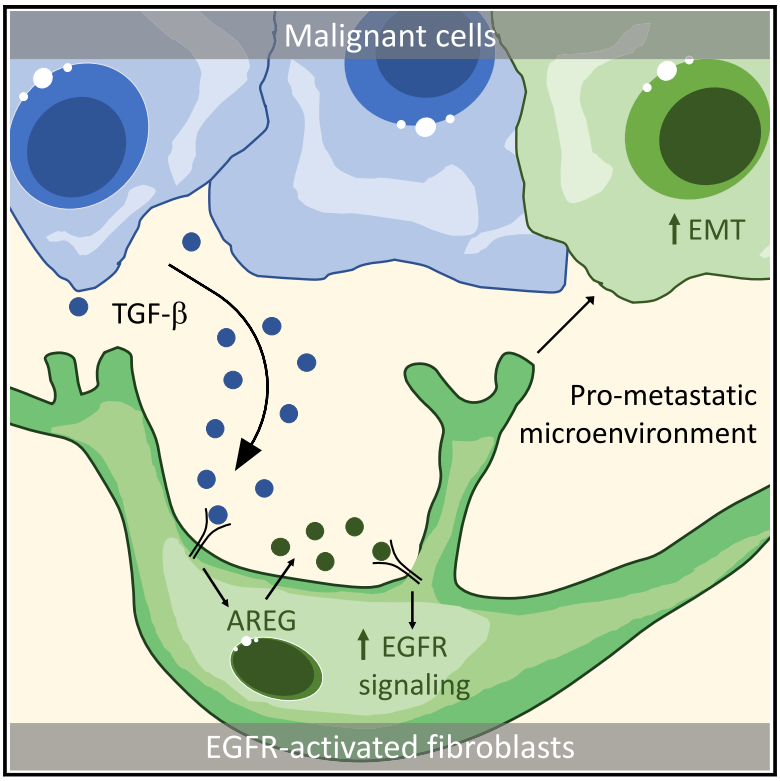

Authors

Gianluca Mucciolo, Joaquín Araos Henríquez, Muntadher Jihad, ..., Ashley Sawle, Anna Piskorz, Giulia Biffi

Correspondence

giulia.biffi@cruk.cam.ac.uk

In brief

Mucciolo et al. demonstrate EGFR/ERBB2 signaling activation in myofibroblastic cancer-associated fibroblasts (myCAFs) in pancreatic ductal adenocarcinoma (PDAC). EGFR-activated myCAFs promote metastasis in PDAC mouse models, revealing a previously unappreciated functional complexity of myCAFs. This knowledge could be used to design therapies that target PDAC malignant cells and tumor-promoting fibroblast populations.

Highlights

- PDAC malignant cell-secreted TGF-β induces EGFR/ERBB2 activation in myCAFs
- EGFR/ERBB2 activation in TGF-β-induced myCAFs is mediated by autocrine amphiregulin
- EGFR/ERBB2 inhibition targets a CD90^{-} myCAF subset in PDAC tumors
- EGFR-activated myCAFs promote PDAC metastasis

Mucciolo et al., 2024, Cancer Cell *42*, 101–118
January 8, 2024
https://doi.org/10.1016/j.ccell.2023.12.002

CellPress

Cancer Cell

CellPress
OPEN ACCESS

Article

EGFR-activated myofibroblasts promote metastasis of pancreatic cancer

Gianluca Mucciolo,[1,2] Joaquín Araos Henríquez,[1,2] Muntadher Jihad,[1] Sara Pinto Teles,[1] Judhell S. Manansala,[1] Wenlong Li,[1] Sally Ashworth,[1] Eloise G. Lloyd,[1] Priscilla S.W. Cheng,[1] Weike Luo,[1] Akanksha Anand,[1] Ashley Sawle,[1] Anna Piskorz,[1] and Giulia Biffi[1,3,*]

[1]University of Cambridge, Cancer Research UK Cambridge Institute, Li Ka Shing Centre, Robinson way, Cambridge CB2 0RE, UK
[2]These authors contributed equally
[3]Lead contact
*Correspondence: giulia.biffi@cruk.cam.ac.uk
https://doi.org/10.1016/j.ccell.2023.12.002

SUMMARY

Pancreatic ductal adenocarcinoma (PDAC) has a dismal prognosis. Cancer-associated fibroblasts (CAFs) are recognized potential therapeutic targets, but poor understanding of these heterogeneous cell populations has limited the development of effective treatment strategies. We previously identified transforming growth factor beta (TGF-β) as a main driver of myofibroblastic CAFs (myCAFs). Here, we show that epidermal growth factor receptor/Erb-B2 receptor (EGFR/ERBB2) signaling is induced by TGF-β in myCAFs through an autocrine process mediated by amphiregulin. Inhibition of this EGFR/ERBB2-signaling network in PDAC organoid-derived cultures and mouse models differentially impacts distinct CAF subtypes, providing insights into mechanisms underpinning their heterogeneity. Remarkably, EGFR-activated myCAFs promote PDAC metastasis in mice, unmasking functional significance in myCAF heterogeneity. Finally, analyses of other cancer datasets suggest that these processes might operate in other malignancies. These data provide functional relevance to myCAF heterogeneity and identify a candidate target for preventing tumor invasion in PDAC.

INTRODUCTION

Pancreatic ductal adenocarcinoma (PDAC) is projected to be the second most common cause of cancer-related death by 2030.[1] PDAC is frequently lethal because it is often diagnosed late after patients have developed metastases. Dissecting metastatic mechanisms in PDAC and ways to prevent and treat this is therefore a priority. More than any other cancer, PDAC is characterized by an abundant, non-malignant stroma that promotes cancer growth and treatment resistance. The majority of this stroma comprises a heterogeneous population of cancer-associated fibroblasts (CAFs),[2–10] including molecularly and potentially functionally diverse myofibroblastic CAFs (myCAFs), inflammatory CAFs (iCAFs) and antigen-presenting CAFs (apCAFs).[6,9,11] Genetic depletion or pharmacological targeting of distinct CAF populations leads to different outcomes, highlighting the need to better understand the signaling pathways that maintain the identity and function of tumor-promoting CAFs.[4,8,12–16] This work is required to unmask effective PDAC treatment strategies.

We previously identified interleukin 1 (IL-1) and transforming growth factor β (TGF-β) as the principal malignant cell-derived ligands that induce iCAF and myCAF formation, respectively.[3] While knowledge of pathways downstream of IL-1 signaling has revealed iCAF treatment targets, pathways active in TGF-β-induced myCAFs are largely unknown.

RESULTS

TGF-β and PDAC organoid-conditioned media activate EGFR/ERBB2 signaling in myCAFs

TGF-β signaling is known to promote the formation and proliferation of PDAC myCAFs, but it is not known if this pathway serves other functions in these cells.[3] Therefore, we characterized receptor tyrosine kinase (RTK) phosphorylation following exposure of PDAC CAF precursor cells—pancreatic stellate cells (PSCs)[9,16]—to TGF-β. Phosphorylated epidermal growth factor receptor (p-EGFR) and phosphorylated Erb-B2 receptor (p-ERBB2) were the most abundant RTKs activated upon TGF-β treatment, and their levels significantly increased compared to quiescent PSCs cultured in control media (Figures 1A and 1B). EGFR activation following TGF-β treatment was confirmed by western blotting in human PSCs (Figure S1A). Additionally, analysis of single-cell RNA-sequencing (scRNA-seq) datasets[6] confirmed EGFR and ERBB2 expression in murine and human PDAC CAFs *in vivo* (Figures S1B and S1C).

Deletion of TGF-β receptor II (TGFBR2) from PSCs blocked the induction of TGF-β responsive genes, TGF-β-dependent proliferation and activation of EGFR (Figures 1C and S1D–S1F). This suggests that TGF-β activates EGFR via its cognate receptor TGFBR2. Additionally, activation of EGFR and ERBB2 in PSCs was rapid, sustained and sensitive to TGF-β receptor I

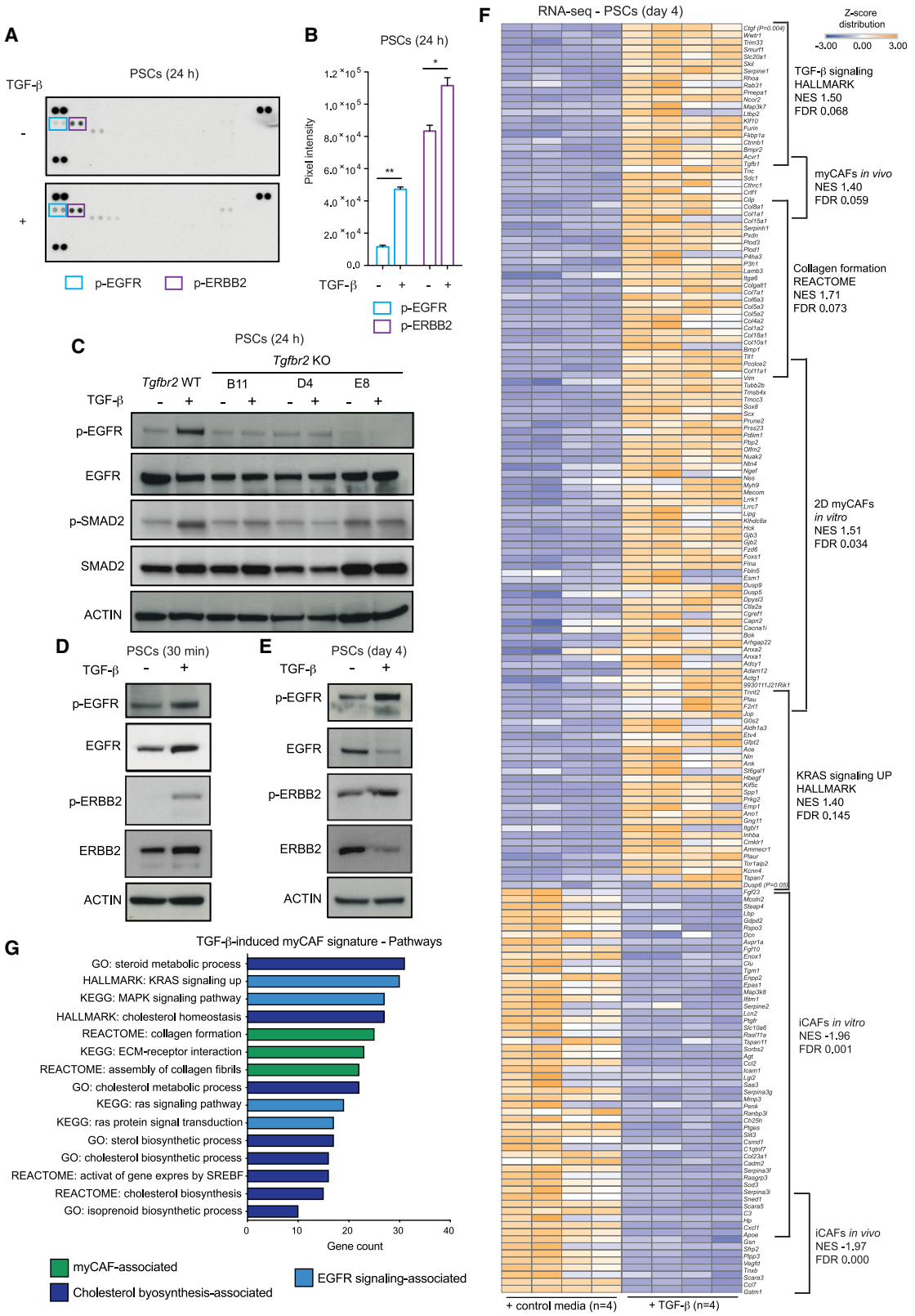

Figure 1. TGF-β activates EGFR/ERBB2 signaling in myCAFs

(A) Receptor tyrosine kinase (RTK) phosphorylation analysis of murine pancreatic stellate cells (PSCs) cultured for 24 h in Matrigel in control media with or without 20 ng/mL TGF-β. Blue and purple boxes highlight p-EGFR and p-ERBB2, respectively.

(legend continued on next page)

(TGFBR1) inhibition (TGFBR1i) (Figures 1D, 1E, and S1G). Furthermore, *Erbb2* deletion in PSCs led to impaired TGF-β-dependent EGFR activation, suggesting that EGFR and ERBB2 cooperate to activate signaling downstream (Figures S1H–S1J).

As sustained EGFR/ERBB2 activation was still observed after 4 days of treatment with TGF-β, we performed RNA-sequencing (RNA-seq) of TGF-β-treated PSCs and controls at this timepoint. In keeping with its previously shown capacity to induce a myCAF phenotype,[3] TGF-β-treated PSCs were enriched for known myCAF-associated pathways, including extracellular matrix (ECM)-associated and TGF-β-dependent LRRC15$^+$ CAF signatures,[5,12] and depleted for known iCAF signatures (Figures 1F, 1G, and S1K; Table S1).[5,6,9,14] These results validated our rationale of analyzing TGF-β-treated PSCs to look at signaling pathways activated in myCAFs. Moreover, this analysis revealed a significant enrichment of cholesterol biosynthesis-associated signatures in TGF-β-induced myCAFs (Figure 1G). Additionally, TGF-β-treatment of PSCs also induced signatures associated with EGFR activation, including KRAS signaling, MAPK signaling and increased expression of *Dusp6*, a known target of the ERK pathway[17] (Figures 1F and 1G; Table S1). Notably, *Dusp6* expression, KRAS signaling and the TGF-β-induced myCAF signature were also enriched in murine myCAFs compared to iCAFs in PDAC *in vivo* (Figures S1L and S1M).

TGF-β is expressed by PDAC malignant cells *in vitro* and *in vivo* (Figures S1N–S1P). Additionally, we previously showed that PDAC organoid-conditioned media (CM) activate SMAD2, a downstream member of the TGF-β pathway, in PSCs, and that inhibition of TGF-β signaling in CM-treated PSCs enhances the iCAF phenotype.[3] Together, these observations suggest that treatment of PSCs with PDAC organoid CM activates myCAF features. Therefore, we assessed whether PDAC organoid CM activate EGFR/ERBB2 signaling in PSCs, after confirming that PDAC organoids secrete TGF-β (Figure S1Q). PDAC organoid CM induced EGFR and ERBB2 activation in PSCs, which was blocked by the dual EGFR and ERBB2 receptor inhibitor (ERBBi) neratinib (Figure 2A). In addition to TGF-β, PDAC organoids also expressed EGFR/ERBB2 ligands that may contribute to boosting EGFR/ERBB2 activation in myCAFs (Figure S1R).

To better characterize EGFR/ERBB2-activated CAFs, we performed RNA-seq of PSCs treated with CM in the presence or absence of ERBBi. By intersecting genes induced by both TGF-β and CM with genes downregulated by EGFR/ERBB2 inhibition, we defined a 52-gene *in vitro* myCAF-derived ERBB signature (Figure 2B; Table S2). PSCs treated with CM upregulated KRAS signaling and *Dusp6* expression, and these effects were blocked by ERBBi without significantly altering TGF-β signaling activation (Figures 2C, 2D, and S1S; Table S2). Furthermore, cholesterol biosynthesis-associated signatures were among the most significantly enriched pathways in the myCAF-derived ERBB signature (Figures 2C and 2D; Table S2), and both the myCAF-derived ERBB signature and the cholesterol biosynthesis signature were also upregulated in myCAFs *in vivo* (Figure S2A). Finally, in keeping with a TGF-β/EGFR signaling network in myCAFs, and further validating our findings, gene set variation analysis (GSVA) of The Cancer Genome Atlas (TCGA) dataset for PDAC (PAAD) identified a significant positive correlation between the human myCAF signature,[6] myCAF-associated TGF-β and Hedgehog (HH) gene signatures,[3,18] and EGFR and ERK signaling (Figure S2B).

Together, these data support a model in which PDAC malignant cell-secreted TGF-β activates EGFR signaling in myCAFs in murine and human PDAC.

TGF-β-induced autocrine amphiregulin activates EGFR signaling in myCAFs

Early activation of EGFR signaling in PSCs following treatment with TGF-β for 30 min appeared to be mediated by increased receptor expression rather than ligand production (Figures 1D and S2C). To investigate how EGFR activation is sustained in TGF-β-induced myCAFs, we looked for expression of known EGFR/ERBB2 ligands in RNA-seq profiles of PSCs cultured with TGF-β or PDAC organoid CM in the presence or absence of ERBBi. These RNA-seq profiles identified EGFR/ERBB2 ligands, including amphiregulin (*Areg*) and heparin binding EGF-like growth factor (*Hbegf*), significantly induced by TGF-β (Figure 2E). Reverse transcription quantitative polymerase chain reaction (RT-qPCR) analysis confirmed TGF-β-induced expression of *Areg* and *Hbegf* in PSCs that was blocked by knockout (KO) of *Tgfbr2* or treatment with the TGFBR1 inhibitor (TGFBR1i) A83-01 (Figures 2F and S2D). Moreover, only partial loss of *Areg* and *Hbegf* expression was observed following genetic deletion or pharmacological inhibition of *Egfr* or *Erbb2*, validating *Areg* and *Hbegf* as candidate mediators of EGFR activation in TGF-β-induced myCAFs *in vitro* (Figures 2F and S2D–S2H). However, *Areg* was the only EGFR/ERBB2 ligand significantly induced by both TGF-β and PDAC organoid CM treatments (Figure 2E). Furthermore, only *AREG*, not *HBEGF*, expression was positively correlated with *TGFB1* expression in TCGA PAAD transcriptomes, suggesting AREG as the likely mediator of TGF-β-induced EGFR signaling activation in myCAFs (Figure S2I). In addition, we confirmed upregulation of AREG protein by TGF-β in PSCs, which was fully blocked by *Tgfbr2* deletion or

(B) Quantification of p-EGFR and p-ERBB2 levels from (A). Results show mean ± standard deviation (SD) of n = 2 technical replicates. *, $p < 0.05$; **, $p < 0.01$, unpaired Student's *t* test.

(C) Western blot analysis of p-EGFR, EGFR, p-SMAD2 and SMAD2 in murine *Tgfbr2* wild-type (WT, i.e., *Rosa26* KO) and knock out (KO) PSCs (3 clones from 3 different guide RNAs) cultured for 24 h in Matrigel in control media with or without 20 ng/mL TGF-β.

(D and E) Western blot analysis of p-EGFR, EGFR, p-ERBB2, and ERBB2 in murine PSCs cultured for (D) 30 min or (E) 4 days in Matrigel in control media with or without 20 ng/mL TGF-β.

(F) RNA-seq of PSCs cultured for 4 days in Matrigel in control media with or without 20 ng/mL TGF-β (n = 4/group). The myCAF and iCAF *in vitro* and *in vivo* signatures were obtained from Öhlund et al.[9] and Elyada et al.,[6] respectively. NES, normalized enrichment score; FDR, false discovery rate. p, unpaired Student's *t* test.

(G) Pathways shown were found significantly enriched (FDR < 0.05) in the TGF-β-induced myCAF signature by DAVID analysis. The TGF-β-induced myCAF signature includes 747 genes defined with LogFC > 1 and FDR < 0.05 in PSCs cultured with TGF-β compared to PSCs cultured in control media. See also Figure S1 and Table S1.

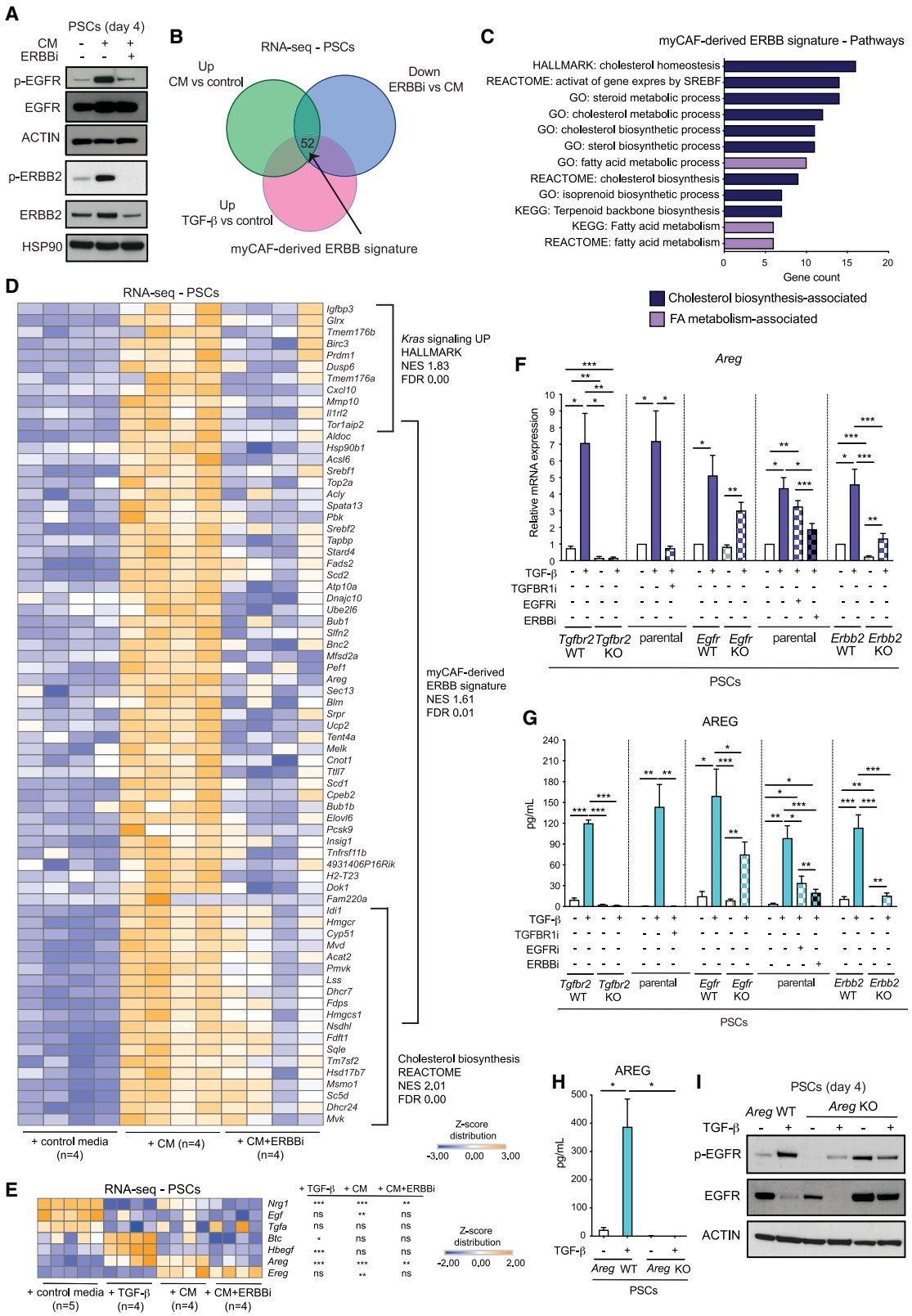

Figure 2. TGF-β-induced autocrine amphiregulin activates EGFR signaling in myCAFs

(A) Western blot analysis of p-EGFR, EGFR, p-ERBB2, and ERBB2 in murine PSCs cultured for 4 days in Matrigel in control media or PDAC organoid-conditioned media (CM) with or without 300 nM EGFR/ERBB2 inhibitor (ERBBi) neratinib.

(legend continued on next page)

TGFBR1 pharmacological inhibition, but not by *Egfr* or *Erbb2* deletion or inhibition (Figure 2G). Finally, scRNA-seq analysis confirmed higher expression of *Areg* in PDAC myCAFs compared to iCAFs *in vivo* (Figures S2J–S2L).

To test directly whether AREG mediated the activation of EGFR signaling in TGF-β-induced myCAFs, we deleted the *Areg* gene from PSCs (Figure 2H). Sustained EGFR activation induced by TGF-β was decreased in *Areg* KO PSCs relative to controls (Figure 2I). Notably, in agreement with our previous results, loss of AREG did not blunt the early activation of EGFR following TGF-β treatment, supporting the notion that this is a ligand-independent phenomenon (Figure S2M). Finally, treatment with AREG alone did neither induce the expression of *Dusp6* or TGF-β target genes nor activate EGFR signaling in PSCs (Figures S2N–S2P). These results further support a model in which activation of the TGF-β pathway upstream AREG induction is required for effective EGFR signaling activation in PDAC myCAFs.

Thus, autocrine AREG mediates EGFR activation downstream of TGF-β signaling in PDAC myCAFs.

Inhibition of EGFR/ERBB2 signaling depletes myCAFs *in vitro*

To further understand how EGFR/ERBB2 activation impacts myCAFs, we first measured the proliferation of PSCs following TGF-β or PDAC organoid CM treatment in the presence of EGFR and/or EGFR/ERBB2 inhibitors. PSC proliferation was reduced significantly following both immediate or delayed (72 h) exposure to EGFRi and/or ERBBi without a detectable increase in apoptosis, suggesting that EGFR/ERBB2 signaling mediates the proliferation of TGF-β-induced myCAFs (Figures 3A, 3B, and S3A–S3F). This was in accordance with reduced TGF-β-dependent proliferation of PSCs following *Egfr* or *Erbb2* deletion (Figures S1I, S2F, and S2G).

PDAC CAFs co-exist in different states.[4] Therefore, we set to evaluate the effect of EGFR/ERBB2 inhibition on CAF composition in the presence of both myCAFs and iCAFs *in vitro* to more closely model the *in vivo* situation. To this end, we cultured PSCs with PDAC organoid CM in the presence or absence of ERBBi, since treatment with CM not only activates TGF-β signaling but also induces IL-1 signaling and iCAF marker expression.[3] Known iCAF-associated signatures,[3,6] including JAK/STAT signaling, NF-κB signaling and the *in vivo* iCAF signature, were not significantly altered by EGFR/ERBB2 inhibition (Figures S3G and S3H). Additionally, the hypoxia signature, which has been recently described as an iCAF feature *in vitro* and *in vivo*,[6,19] was increased upon EGFR/ERBB2 inhibition (Figures 3C and S3G; Table S2). On the contrary, in keeping with the finding that EGFR/ERBB2 activation occurs in myCAFs, EGFR/ERBB2 inhibition downregulated known myCAF-associated signatures (Figures 3C and S1L). Furthermore, signatures of previously identified myCAF subsets,[5,14] including TGF-β-dependent LRRC15^{+} CAFs,[5,12] were not significantly affected by EGFR/ERBB2 inhibition (Figure S3I). RT-qPCR analysis confirmed an upregulation of iCAF markers[3] upon EGFR/ERBB2 inhibition (Figures 3D and S3J). This effect was also observed when PSCs and PDAC organoids were co-cultured in transwell, even if PDAC organoid proliferation was reduced by treatment with ERBBi (Figures 3E and S3K). To further evaluate the impact of EGFR signaling blockade on iCAFs and myCAFs *in vitro*, we analyzed by RT-qPCR *Egfr* wild-type (WT, i.e., *Rosa26* KO) and *Egfr* KO PSCs treated with PDAC organoid CM. This analysis showed that only the expression of myCAF markers was downregulated in *Egfr* KO PSCs compared to *Egfr* WT PSCs, while the induction of iCAF markers was not affected by *Egfr* deletion alone (Figure S3L). This suggests that combined EGFR/ERBB2 blockade is required for effective targeting of EGFR-activated myCAFs.

To analyze a model even closer to the *in vivo* situation, we established co-cultures of PDAC organoids with *Egfr* WT or *Egfr* KO PSCs. Flow-sorted malignant cell and PSC populations were then analyzed by RNA-seq (Figures 3F and 3G). Known myCAF-associated signatures comprised the majority of downregulated pathways in *Egfr*-deleted PSCs compared to controls (Figure 3H; Table S3). While the hypoxia and *in vitro* iCAF signatures were also downregulated, this could be due to changes in co-cultured malignant cells, rather than to a direct effect of *Egfr* loss, since EGFR/ERBB2 inhibition upregulated the hypoxia signature and iCAF markers in PSCs cultured with CM. Furthermore, the *in vivo* iCAF signature and pathways known to induce and maintain the iCAF phenotype, such as JAK/STAT and NF-κB signaling, were not significantly altered in *Egfr*-deleted PSCs compared to controls (Figure S3M). Finally, as observed following EGFR/ERBB2 inhibition, signatures of previously

(B) Venn diagrams showing the overlap between significantly upregulated genes in PSCs cultured with PDAC organoid CM compared to PSCs cultured with control media, significantly downregulated genes in PSCs cultured with PDAC organoid CM + 300 nM ERBBi compared to PSCs cultured with CM and significantly upregulated genes in PSCs cultured with TGF-β compared to PSCs cultured with control media, as assessed by RNA-seq. The 52 genes common to all three groups comprise the myCAF-derived ERBB signature (i.e., *in vitro* myCAF-derived EGFR/ERBB2 signature).

(C) Pathways shown were found significantly enriched (FDR < 0.05) in the myCAF-derived ERBB signature from (B) by DAVID analysis.

(D) RNA-seq of PSCs cultured for 4 days in Matrigel in control media or CM with or without ERBBi (n = 4/group). NES and FDR values shown refer to the CM vs. control media comparison.

(E) RNA-seq expression of known EGFR/ERBB ligands (*Nrg1*, *Egf*, *Tgfa*, *Btc*, *Hbegf*, *Areg*, and *Ereg*) in PSCs cultured for 4 days in Matrigel in control media or with 20 ng/mL TGF-β or PDAC organoid CM or CM with 300 nM ERBBi (n = 4–5/group). The TGF-β and CM significance was calculated compared to the control media condition, the CM + ERBBi significance was calculated compared to the CM condition.

(F and G) (F) qPCR analysis of *Areg* or (G) enzyme-linked immunosorbent assay (ELISA) of AREG in murine parental (i.e., unmodified), WT (i.e., *Rosa26* KO), *Tgfbr2* KO, *Egfr* KO and *Erbb2* KO PSCs cultured for 4 days in Matrigel in control media with or without 20 ng/mL TGF-β in the presence or absence of 1 μM erlotinib (EGFRi) or 300 nM neratinib (ERBBi) or 2 μM A83-01 (TGFBR1i). Results show mean ± SEM of n = 4–14 (F) or n = 4–13 (G) biological replicates.

(H) ELISA of AREG from media of murine *Areg* WT (i.e., *Rosa26* KO) and KO PSCs cultured for 4 days in Matrigel in control media with or without 20 ng/mL TGF-β. Results show mean ± SEM of n = 4 biological replicates (and n = 2–3 technical replicates).

(I) Western blot analysis of p-EGFR and EGFR in murine *Areg* WT and KO PSCs (2 clones from 2 different guide RNAs) cultured for 4 days in Matrigel in control media with or without 20 ng/mL TGF-β. (E, F, G, and H) *, $p < 0.05$; **, $p < 0.01$, ***, $p < 0.001$, paired and unpaired Student's *t* test. See also Figure S2 and Table S2.

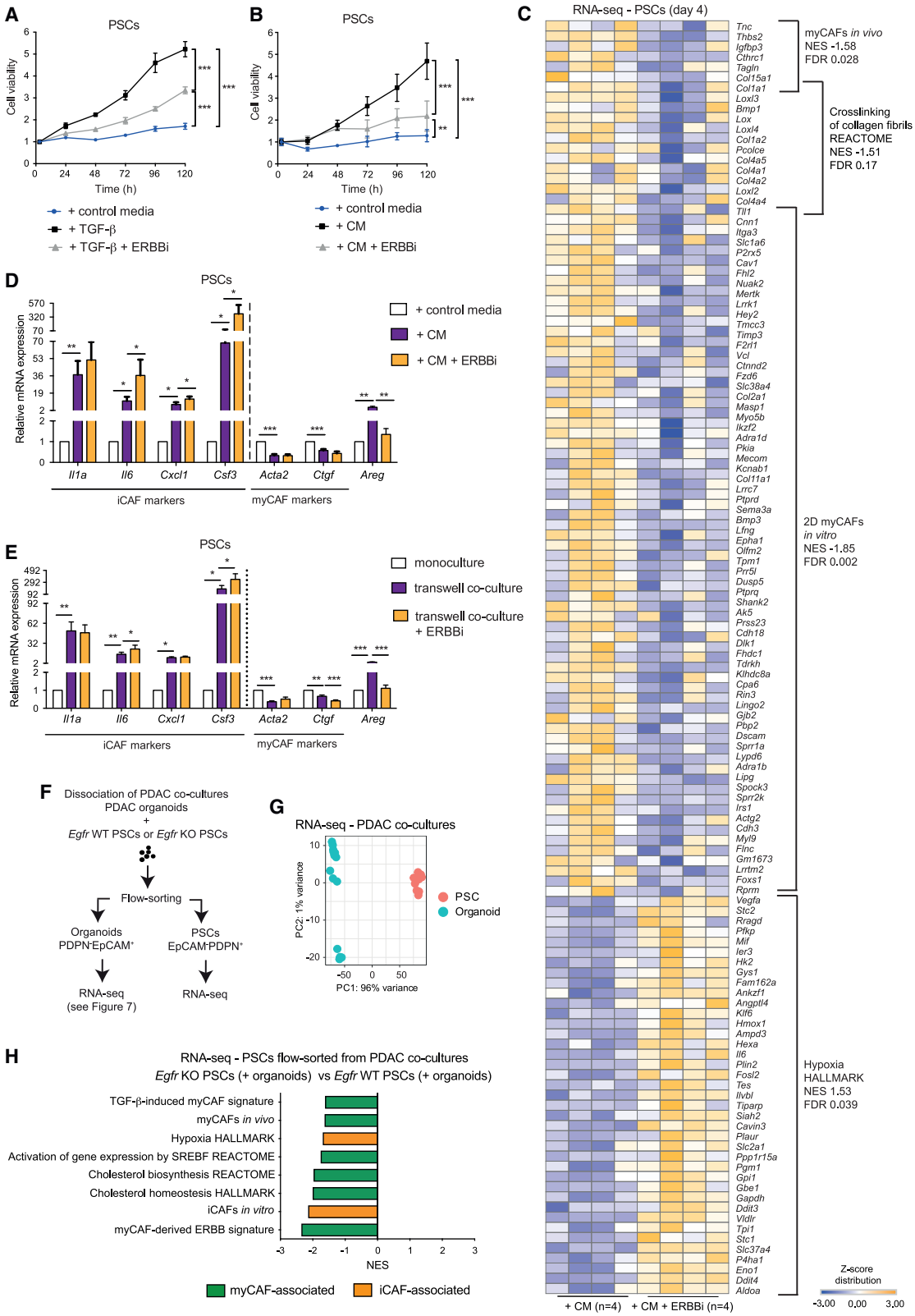

Figure 3. Inhibition of EGFR/ERBB2 signaling depletes myCAFs *in vitro*

(A) Proliferation curves of murine PSCs cultured for 120 h in Matrigel in control media with or without 20 ng/mL TGF-β in the presence or absence of 300 nM neratinib (ERBBi). n = 3 biological replicates (with n = 3–5 technical replicates each).

(legend continued on next page)

identified myCAF subsets,[5,14] including TGF-β-dependent LRRC15$^+$ CAFs,[5,12] were not significantly affected by *Egfr* deletion (Figure S3N).

Altogether these data demonstrate that EGFR/ERBB2 inhibition preferentially targets myCAFs over iCAFs *in vitro*, and suggest that only a subset of myCAFs is depleted. Additionally, these analyses highlight how combined EGFR/ERBB2 inhibition, rather than EGFR blockade alone, may be required for effective targeting of EGFR-activated myCAFs *in vivo*.

Inhibition of EGFR/ERBB2 signaling preferentially targets myCAFs *in vivo*

To determine whether EGFR/ERBB2 signaling inhibition differentially affects distinct CAF subtypes *in vivo*, we established orthotopic transplantation mouse models with PDAC organoids and treated tumor-bearing mice for 2 weeks with the EGFR/ERBB2 inhibitor (ERBBi) neratinib (Figure 4A). Effective targeting of the EGFR pathway was confirmed by downregulation of p-EGFR and *Areg* levels and increased T cell and CD8$^+$ T cell abundance, which was previously reported following treatment with the EGFR inhibitor erlotinib[20] (Figures S4A–S4F). EGFR/ERBB2 inhibition did not alter the abundance of other immune cell populations, such as neutrophils and macrophages, or of endothelial cells, epithelial cells and total CAFs (Figures S4G–S4I). To evaluate whether EGFR/ERBB2 inhibition *in vivo* differentially impacted distinct subsets of CAFs, we leveraged our established flow cytometric quantification of Ly6C$^-$MHCII$^-$ myCAFs, Ly6C$^+$MHCII$^-$ iCAFs and LY6C$^-$MHCII$^+$ apCAFs[6] (Figure S4J). While apCAFs were not significantly altered, myCAFs were reduced and iCAFs were increased upon ERBBi treatment, significantly altering the myCAF/non-myCAF ratio in PDAC tumors (Figures 4B, 4C, and S4K). While CAFs have been shown to interconvert upon pharmacological inhibition of pathways important for their formation,[3,9] whether this is relevant to our observations remains to be determined.

To further investigate the effect of EGFR/ERBB2 inhibition on CAFs, we established additional PDAC organoid-derived orthotopic transplantation mouse models and treated tumor-bearing mice for 2 weeks with either ERBBi or vehicle, prior to flow-sorting both malignant cell and fibroblast populations for RNA-seq analysis (Figures 4A and 4D). In keeping with the finding that EGFR/ERBB2 activation occurs in myCAFs, CAFs from ERBBi-treated tumors significantly downregulated *Areg* expression and the TGF-β-induced myCAF signature and significantly upregulated the *in vivo* iCAF signature compared to CAFs from vehicle-treated tumors (Figures 4E and S4L–S4N; Table S4). Furthermore, signatures of previously identified myCAF subsets,[5,14] including TGF-β-dependent LRRC15$^+$ CAFs,[5,12] were not significantly affected by ERBBi treatment, indicating that EGFR/ERBB2 inhibition may only deplete a subset of myCAFs (Figure S4M).

To validate our findings and further investigate CAF population changes following EGFR/ERBB2 inhibition, we performed single-nuclei RNA-sequencing (snRNA-seq) on PDAC tumors treated for 2 weeks with either ERBBi or vehicle (Figure 4A, 4F, 4G, and S4O–S4Q). Downregulation of *Dusp6* expression confirmed targeting of the pathway across multiple cell types, and analysis of differentially expressed genes identified epithelial cells and CAFs as most affected cell populations following EGFR/ERBB2 inhibition (Figures 4H and S4R). Notably, iCAF abundance and iCAF-associated signatures were enriched in ERBBi-treated PDAC tumors compared to vehicle-treated tumors, whereas myCAF abundance and myCAF-associated signatures were downregulated (Figures 4I–4L and S4S; Table S4).

Finally, while primary tumor growth and incidence of ascites and liver metastases were not significantly affected, EGFR/ERBB2 inhibition led to significantly less mice with diaphragm and lung metastases (Figures 4M and S4T–S4V).

Altogether, these data demonstrate *in vivo* targeting of myCAFs following EGFR/ERBB2 inhibition in PDAC, and indicate that EGFR/ERBB2 pathway inhibition in a subset of myCAFs may impair PDAC metastasis formation.

Inhibition of EGFR/ERBB2 signaling depletes a subset of myCAFs

While our data suggest a potential metastasis-promoting role of EGFR-activated myCAFs in PDAC, previous findings have shown that α-smooth muscle actin (αSMA)-positive or HH-activated myofibroblasts and ECM components, such as collagen, restrain PDAC progression.[13,15,21] However, in contrast to these previous studies and TGF-β[3] or HH[18] signaling inhibition, ERBBi treatment did not reduce overall collagen deposition or levels of the myofibroblastic marker αSMA (Figures 5A–5C). Therefore, we evaluated whether EGFR/ERBB2 inhibition only targets a subset of myCAFs in PDAC tumors. We previously found that *Thy1* (coding for CD90) is highly expressed in myCAFs compared to iCAFs and apCAFs[6] (Figure S5A). However, *Thy1* expression in myCAFs was heterogeneous and marked only a subset of myCAFs (Figures S5B–S5D). Therefore, to start to investigate potential differential impact of ERBBi treatment on subsets of

(B) Proliferation curves of murine PSCs cultured for 120 h in Matrigel in control media or PDAC organoid CM in the presence or absence of 300 nM neratinib (ERBBi). n = 2 biological replicates (with n = 5 technical replicates each).
(C) RNA-seq analysis of PSCs cultured for 4 days in Matrigel in CM (n = 4) or CM in the presence of 300 nM neratinib (ERBBi) (n = 4).
(D) qPCR analysis of *Areg*, and iCAF (*Il1a*, *Il6*, *Cxcl1*, and *Csf3*) and myCAF (*Acta2* and *Ctgf*) markers in murine PSCs cultured for 4 days in Matrigel in control media, PDAC organoid CM or CM in the presence of 300 nM neratinib (ERBBi). n = 7–12 biological replicates.
(E) qPCR analysis of *Areg*, and iCAF (*Il1a*, *Il6*, *Cxcl1*, and *Csf3*) and myCAF (*Acta2* and *Ctgf*) markers in murine PSCs cultured for 4 days in Matrigel in monoculture, in transwell culture with murine PDAC organoids or in transwell culture with murine PDAC organoids in the presence of 300 nM neratinib (ERBBi). n = 10 biological replicates.
(F) Schematic of flow-sorting strategy prior to RNA-seq of murine PDAC co-cultures of PDAC organoids with *Egfr* WT or *Egfr* KO PSCs.
(G) Principal component analysis (PCA) of PSCs and PDAC organoids from (F).
(H) Significantly downregulated pathways (i.e., NES < −1.50 and FDR < 0.25) identified by gene set enrichment analysis (GSEA) of *Egfr* KO PSCs (n = 8) compared to *Egfr* WT PSCs (n = 4), both co-cultured with PDAC organoids for 4 days in Matrigel in control media. (C and H) The *in vitro* and *in vivo* CAF signatures were obtained from Öhlund et al.[9] and Elyada et al.,[6] respectively. Results shown as mean ± SD (A and B) or mean ± SEM (D and E), *, $p < 0.05$; **, $p < 0.01$; ***, $p < 0.001$, paired Student's *t* test. See also Figure S3 and Tables S2, S3.

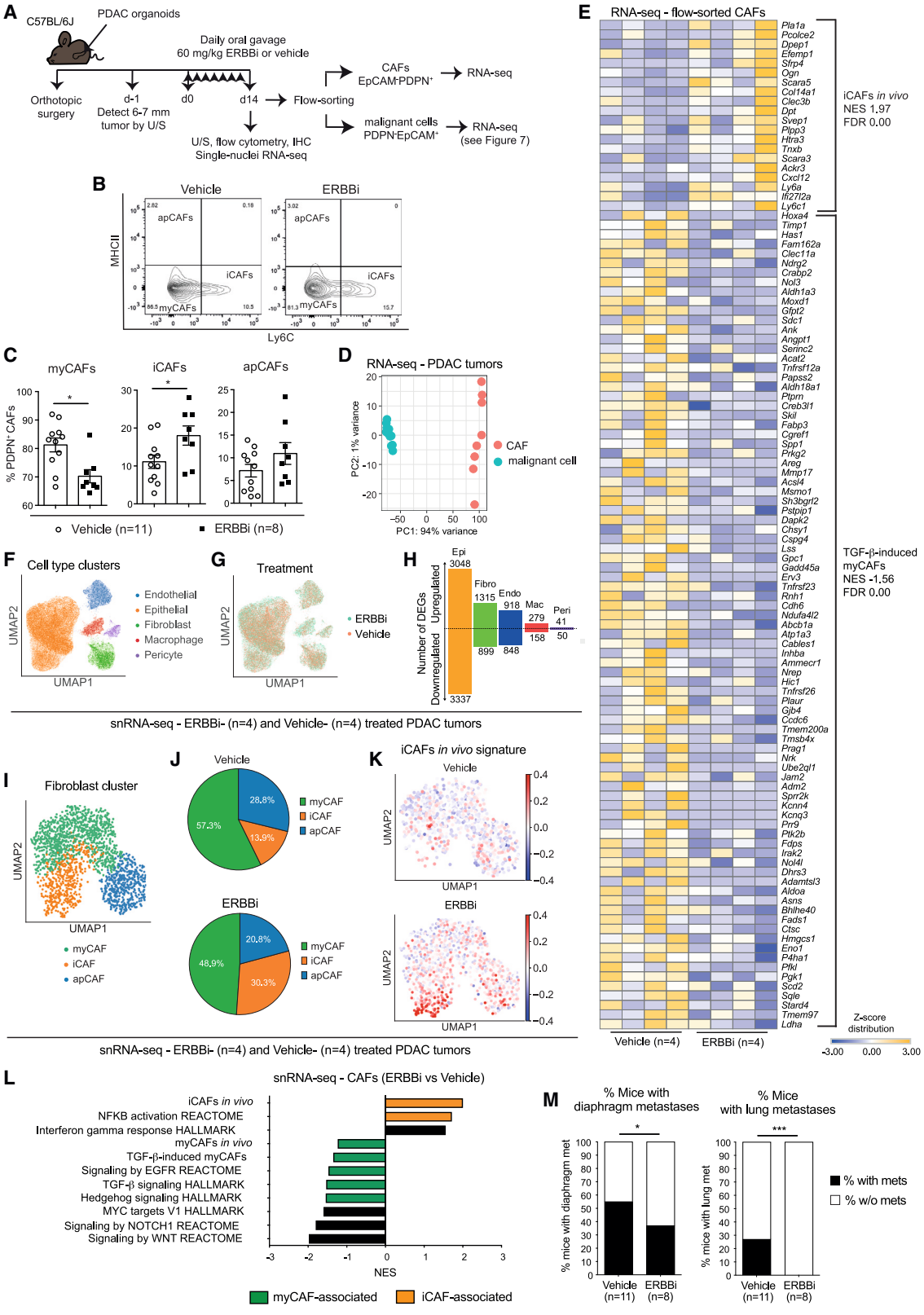

Figure 4. Inhibition of EGFR/ERBB2 signaling preferentially targets myCAFs *in vivo*

(A) Schematic of 2-week treatment of tumor-bearing orthotopically grafted PDAC organoid-derived mouse models with 60 mg/kg ERBBi (neratinib) or vehicle by daily oral gavage, and downstream analyses. U/S, ultrasound.

(legend continued on next page)

myCAFs, we evaluated changes in abundance of CD90$^-$ or CD90$^+$ myCAFs (i.e., CD31$^-$CD45$^-$EpCAM$^-$PDPN$^+$Ly6C$^-$ MHCII$^-$) (Figure S5D). Notably, depletion of myCAFs by EGFR/ERBB2 inhibition was limited to CD90$^-$ myCAFs, while CD90$^+$ myCAFs moderately increased (Figure 5D).

To better characterize CD90$^-$ and CD90$^+$ myCAF populations, we established orthotopically grafted organoid-derived mouse models of PDAC and flow-sorted both myCAF populations prior to RNA-seq (Figures 5E, 5F, and S5D). RNA-seq analysis confirmed successful flow-sorting of both myCAF populations, showing significant downregulation of *Thy1* expression in CD90$^-$ myCAFs compared to CD90$^+$ myCAFs (Figure 5G). Notably, CD90$^-$ myCAFs had significantly higher levels of *Areg* and *Dusp6* compared to CD90$^+$ myCAFs, indicating that EGFR signaling is higher in the CD90$^-$ myCAF subset (Figure 5G). Therefore, these data provide an explanation for preferential targeting of CD90$^-$ myCAFs by EGFR/ERBB2 inhibition. Moreover, CD90$^+$ myCAFs had significantly higher expression of *Acta2* and *Col1a1* compared to CD90$^-$ myCAFs and were enriched in ECM-associated signatures (Figures 5H and 5I; Table S5). Thus, these data suggest that collagen deposition and αSMA levels are not altered following EGFR/ERBB2 inhibition due to targeting of a less ECM-producing CD90$^-$ myCAF population. Furthermore, CD90$^-$ myCAFs were significantly enriched in cholesterol biosynthesis-associated signatures, which are upregulated in TGF-β-induced myCAF and myCAF-derived ERBB signatures *in vitro* (Figures 5I, 1G, and 2C). Additionally, CD90$^-$ myCAFs showed a significant downregulation of known *in vivo* iCAF and myCAF signatures, corroborating their phenotypical difference from CD90$^+$ myCAFs or other previously described myCAF subtypes, including TGF-β-dependent LRRC15$^+$ myCAFs[5,12] (Figures 5I and S5E–S5F). In contrast, the apCAF gene signature, known iCAF-associated signatures, including JAK/STAT and TNF-α signaling, and known myCAF-associated signatures, including TGF-β and HH signaling, did not significantly differ between CD90$^-$ and CD90$^+$ myCAFs (Figures S5G–S5I). Finally, in addition to *Areg*, we identified a number of other secreted proteins differentially expressed in CD90$^-$ and CD90$^+$ myCAFs, which may mediate distinct functions of these CAF populations. Specifically, CD90$^+$ myCAFs were enriched in collagens, which have been shown to play a tumor-restraining role in PDAC,[21] whereas CD90$^-$ myCAFs upregulated genes coding for secreted proteins, including *Spp1* and *Sema3e*, that have been shown to promote metastasis[22,23] (Figures 5J and S5J).

Overall, these data provide insights into myCAF heterogeneity and identify a myCAF subset that is dependent on EGFR/ERBB2 signaling activation and may affect PDAC progression.

EGFR-activated myCAFs promote metastasis of PDAC

Our ERBBi studies in mouse models suggested that EGFR/ERBB2 inhibition in myCAFs may impair PDAC metastasis formation (Figure 4M). However, EGFR signaling in malignant cells has been previously described in PDAC tumorigenesis,[24] and snRNA-seq analysis identified the epithelial cells as the most affected cell types in PDAC tumors following ERBBi treatment (Figure 4H). Moreover, direct cell-cell population effects are challenging to deconvolute in therapeutic studies in which multiple populations can be directly and/or indirectly affected by the treatment. Therefore, to investigate a potential direct role of EGFR-activated myCAFs in PDAC progression, we established orthotopic transplantation mouse models of PDAC organoids alone or co-injected with *Egfr* WT (i.e., *Rosa26* KO) or *Egfr* KO PSCs (Figure 6A). Detection by immunohistochemistry (IHC) of co-transplanted PSCs, which are immortalized with the SV40 large T antigen, confirmed the role of EGFR signaling in promoting CAF proliferation, as observed *in vitro* (Figures S6A and S6B). Similar to ERBBi- and vehicle-treated PDAC tumors, macrophage and neutrophil infiltration, collagen deposition and αSMA levels were not significantly different across cohorts (Figures S6C and S6D). Flow cytometry analysis showed a decrease in total CAF abundance in PDAC+*Egfr* KO PSC tumors compared to PDAC+*Egfr* WT PSC tumors (Figure S6E). However, this decrease in CAFs was not irrespective of distinct CAF subsets, as only myCAFs were significantly downregulated in PDAC+*Egfr* KO PSC tumors compared to PDAC+*Egfr* WT PSC tumors, altering the myCAF/iCAF ratio (Figure S6F). Furthermore, we evaluated whether *Egfr* deletion in CAFs alters the proportion of iCAFs and myCAFs within the CAF population. In line with what observed following EGFR/ERBB2 inhibition, PDAC+*Egfr* KO PSC tumors contained fewer myCAFs and, accordingly, more iCAFs compared to PDAC+*Egfr* WT PSC tumors (Figures 6B and 6C). Remarkably, only tumors derived from PDAC+*Egfr* WT PSCs were significantly larger than those from

(B) Representative flow plots of Ly6C$^-$MHCII$^-$ myCAFs, Ly6C$^+$MHCII$^-$ iCAFs and Ly6C$^-$MHCII$^+$ apCAFs from the PDPN$^+$ parental gate in vehicle- and ERBBi-treated PDAC tumors.
(C) Flow cytometric analyses of myCAFs (Ly6C$^-$MHCII$^-$), iCAFs (Ly6C$^+$MHCII$^-$), and apCAFs (Ly6C$^-$MHCII$^+$) from the PDPN$^+$ gate in vehicle- (n = 11) and ERBBi- (n = 8) treated PDAC tumors. Results show mean ± SEM. *, $p < 0.05$, Mann-Whitney test.
(D) PCA of CAFs and malignant cells flow-sorted from vehicle- and ERBBi-treated PDAC tumors, as described in (A).
(E) RNA-seq analysis of CAFs flow-sorted from ERBBi- (n = 4) or vehicle- (n = 4) treated PDAC tumors (from D).
(F) Uniform Manifold Approximation and Projection (UMAP) plot of all cell types identified by single-nuclei RNA-sequencing (snRNA-seq) of ERBBi- (n = 4) or vehicle- (n = 4) treated PDAC tumors, as described in (A).
(G) UMAP plot of ERBBi- (n = 4) or vehicle- (n = 4) treated PDAC tumors from (F) showing the 2 treatment conditions in different colors.
(H) Number of upregulated and downregulated differentially expressed genes (DEGs, FDR < 0.05) in each cell type in ERBBi-treated PDAC tumors (n = 4) compared to vehicle-treated PDAC tumors (n = 4) from (F).
(I) UMAP plot of fibroblasts in ERBBi- (n = 4) or vehicle- (n = 4) treated PDAC tumors from (F).
(J) Pie charts showing proportions of different CAF clusters in ERBBi- or vehicle-treated PDAC tumors from (I).
(K) UMAP plots of CAFs in ERBBi- or vehicle-treated PDAC tumors colored by the normalized expression score of the *in vivo* iCAF gene signature.
(L) Significantly upregulated (i.e., NES > 1.50 and FDR < 0.25) and downregulated (i.e., NES < −1.50 and FDR < 0.25) pathways identified by GSEA of CAFs in ERBBi-treated tumors (n = 4) compared to CAFs in vehicle-treated PDAC tumors (n = 4), as assessed by pseudobulk analysis from the snRNA-seq dataset.
(M) Percentages of vehicle- (n = 11) or ERBBi- (n = 8) treated mouse models of PDAC with or without diaphragm or lung metastases (mets). *, $p < 0.05$; ***, $p < 0.001$, chi-square test. (E, K, and L) The *in vivo* iCAF and myCAF signatures were obtained from Elyada et al.[6] See also Figure S4 and Table S4.

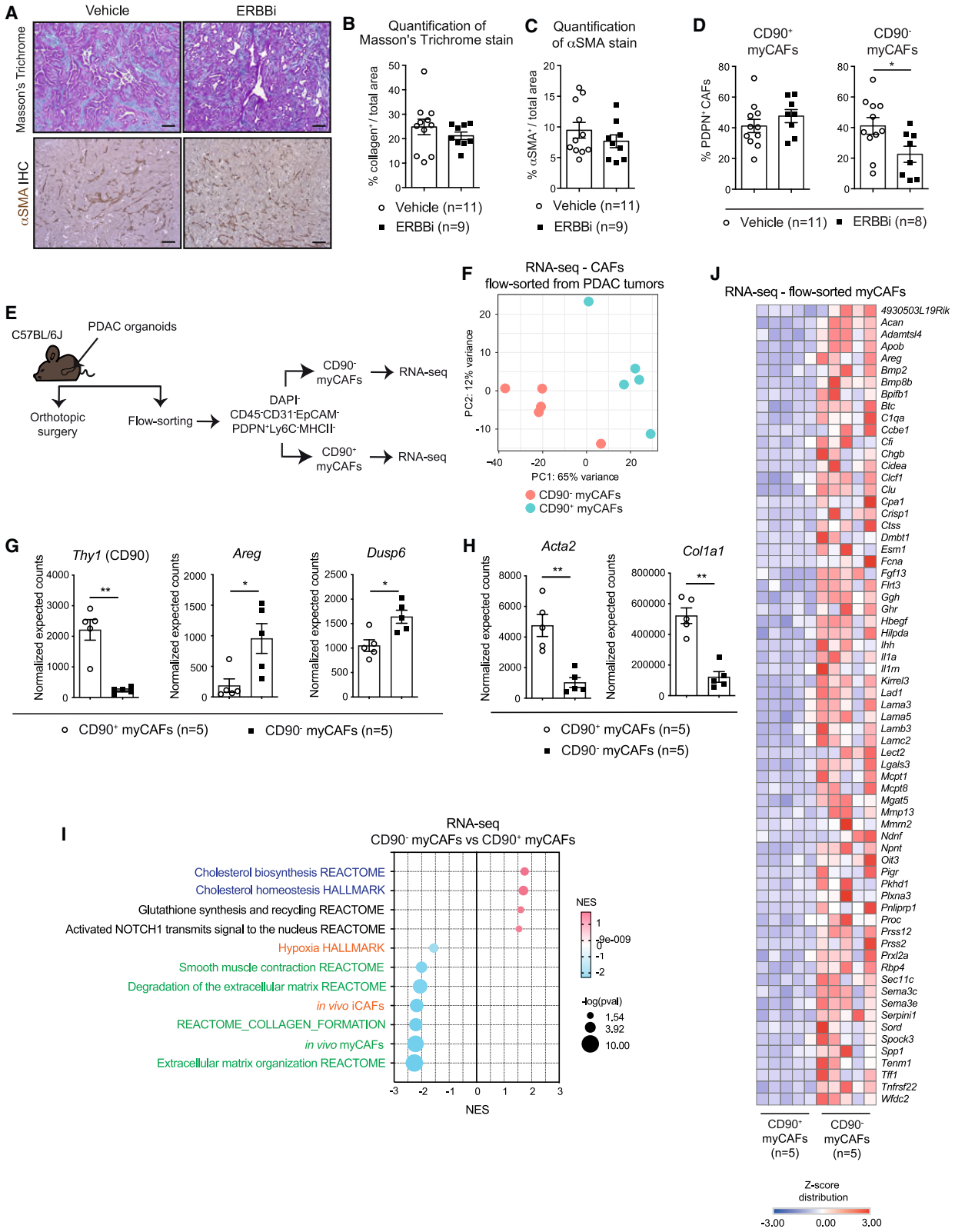

Figure 5. Inhibition of EGFR/ERBB2 signaling depletes a subset of myCAFs

(A) Representative Masson's trichrome and α-smooth muscle actin (αSMA) stains in 2-week vehicle- and ERBBi-treated PDAC tumors, as described in Figure 4A. Scale bars, 50 μm.

(legend continued on next page)

PDAC alone (Figure 6D). Moreover, similar to what observed following EGFR/ERBB2 inhibition, they generated significantly more diaphragm metastases, lung metastases and ascites than PDAC alone or PDAC+*Egfr* KO PSC tumors (Figures 6E–6I). Additionally, mice with PDAC+*Egfr* KO PSC tumors had fewer liver metastases compared to other cohorts (Figures S6G and S6H).

To investigate whether AREG blockade in CAFs would recapitulate the effects of complete EGFR signaling ablation, we established orthotopic transplantation mouse models of PDAC organoids alone or co-injected with *Areg* WT (i.e., *Rosa26* KO) or *Areg* KO PSCs (Figures 6J and S6I). Contrary to what observed in PDAC+*Egfr* KO PSC tumors, PDAC+*Areg* KO PSC tumors had significantly less macrophages compared to PDAC+*Areg* WT PSC tumors (Figures S6J and S6K). These findings are in accordance with our *in vitro* analyses showing that *Egfr* deletion downregulates, but not completely abrogates, *Areg* expression in PSCs (Figures 2F and 2G), and suggest a role for myCAF-produced AREG in fibroblast-macrophage crosstalk. Furthermore, contrary to PDAC+*Egfr* KO PSC tumors, PDAC+*Areg* KO PSC tumors did not significantly differ in overall CAF abundance or iCAF/myCAF proportions compared to PDAC+*Areg* WT PSC tumors (Figures S6L and S6M). These findings are in accordance with our *in vitro* analyses showing that *Areg* deletion impairs, but does not completely inhibit, EGFR signaling activation and, thus, myCAF formation (Figure 2I). Notably, PDAC+*Areg* WT PSC tumors were significantly larger than those derived from PDAC alone or PDAC+*Areg* KO PSCs (Figure 6K). These findings are also in accordance with *in vitro* analyses showing that *Egfr* deletion does not completely blunt *Areg* expression in PSCs, and suggest that myCAF-produced AREG acts locally to promote primary PDAC growth. Finally, *Areg* deletion in PSCs impaired formation of diaphragm metastases, liver metastases and ascites, but had no effect on lung metastases, further highlighting the complexity of CAF-mediated PDAC metastatic processes (Figures 6L–6N and S6N).

Altogether, these data identify a previously unappreciated functional complexity of myCAFs, showing that EGFR-activated myCAFs promote metastasis of PDAC. Furthermore, these results suggest that complete ablation of EGFR signaling activation in CAFs, rather than AREG blockade alone, is required for more effective impairment of their pro-metastatic role.

EGFR-activated myCAFs promote the metastatic potential of PDAC malignant cells

To start to investigate the potential mechanism through which EGFR-activated CAFs promote metastasis of PDAC, we analyzed by RNA-seq PDAC organoids flow-sorted from co-cultures with *Egfr* WT or *Egfr* KO PSCs (Figures 3F and 3G). This analysis revealed significant downregulation of pathways known to be involved in metastasis formation, including the epithelial-to-mesenchymal transition (EMT) and hypoxia gene signatures,[25–27] in organoids cultured with *Egfr*-deficient PSCs compared to organoids cultured with *Egfr*-proficient PSCs (Figure 7A; Table S6). To investigate whether these changes were also observed *in vivo*, we established additional orthotopic transplantation mouse models of PDAC organoids co-injected with *Egfr* WT (i.e., *Rosa26* KO) or *Egfr* KO PSCs and performed RNA-seq on flow-sorted malignant cells (Figures 7B and 7C). Malignant cells flow-sorted from PDAC+*Egfr* KO PSC tumors also showed downregulation of the EMT signature compared to malignant cells flow-sorted from PDAC+*Egfr* WT PSC tumors (Figure 7D; Table S6).

As a complementary strategy, we analyzed changes in the transcriptome of malignant cells following EGFR/ERBB2 inhibition *in vivo*, which depletes EGFR-activated myCAFs. RNA-seq of flow-sorted malignant cells from 2-week ERBBi- or vehicle-treated PDAC tumors confirmed downregulation of metastasis-associated pathways, including EMT and hypoxia gene signatures, following ERBBi treatment (Figures 4A, 4D, 7E, and S7A; Tables S4 and S6). These results were also confirmed by snRNA-seq analysis of PDAC malignant cells in 2-week ERBBi- or vehicle-treated tumors, which showed significant downregulation of EMT and hypoxia gene signatures in epithelial cells of ERBBi-treated tumors compared to vehicle-treated tumors (Figures 4A, 4F–4H, S4O–S4R, 7F, and S7B–S7D; Tables S4 and S6).

Altogether, these data support a role for EGFR-activated myCAFs in promoting PDAC metastasis formation by enhancing the metastatic potential of PDAC malignant cells (Figure 7G).

EGFR activation occurs in myofibroblastic CAFs in various malignancies

As PDAC CAFs share features with CAF subtypes in other malignancies,[4] we investigated the broader impact of our findings among malignancies in which EGFR and/or ERBB2 inhibition is an established therapeutic strategy.[28] Similar to what observed

(B and C) Quantification of Masson's trichrome stain (B) and αSMA stain (C) in 2-week vehicle- (n = 11) and ERBBi- (n = 9) treated PDAC tumors.
(D) Flow cytometric analyses of $CD90^-Ly6C^-MHCII^-$ myCAFs (i.e., $CD90^-$ myCAFs) and $CD90^+Ly6C^-MHCII^-$ myCAFs (i.e., $CD90^+$ myCAFs) from the $PDPN^+$ CAF gate in vehicle- (n = 11) and ERBBi- (n = 8) treated PDAC tumors.
(E) Schematic of flow-sorting strategy and downstream RNA-seq of $CD90^-$ and $CD90^+$ myCAFs from tumors derived from the orthotopic transplantation of PDAC organoids.
(F) PCA of $CD90^-$ and $CD90^+$ myCAFs, as described in (E).
(G) RNA-seq expression of *Thy1* (coding for CD90), *Areg* and *Dusp6* in $CD90^+$ and $CD90^-$ myCAFs flow-sorted from PDAC tumors (n = 5).
(H) RNA-seq expression of *Acta2* and *Col1a1* in $CD90^+$ and $CD90^-$ myCAFs flow-sorted from PDAC tumors (n = 5).
(I) Significantly upregulated (i.e., NES > 1.50 and FDR < 0.25) or downregulated (i.e., NES < −1.50 and FDR < 0.25) pathways identified by GSEA of $CD90^-$ myCAFs compared to $CD90^+$ myCAFs flow-sorted from PDAC tumors (n = 5). The *in vivo* iCAF and myCAF signatures were obtained from Elyada et al.[6] myCAF-associated pathways are highlighted in green; iCAF-associated pathways are highlighted in orange; cholesterol biosynthesis-associated pathways are highlighted in blue.
(J) RNA-seq analysis of significantly upregulated (LogFC > 1 and FDR < 0.05) genes coding for secreted proteins in $CD90^-$ myCAFs compared to $CD90^+$ myCAFs from PDAC tumors (n = 5). The list of mouse secreted proteins was obtained from UniProt. (B, C, D, G, and H) Results show mean ± SEM. *, $p < 0.05$; **, $p < 0.01$, Mann-Whitney test. See also Figure S5 and Table S5.

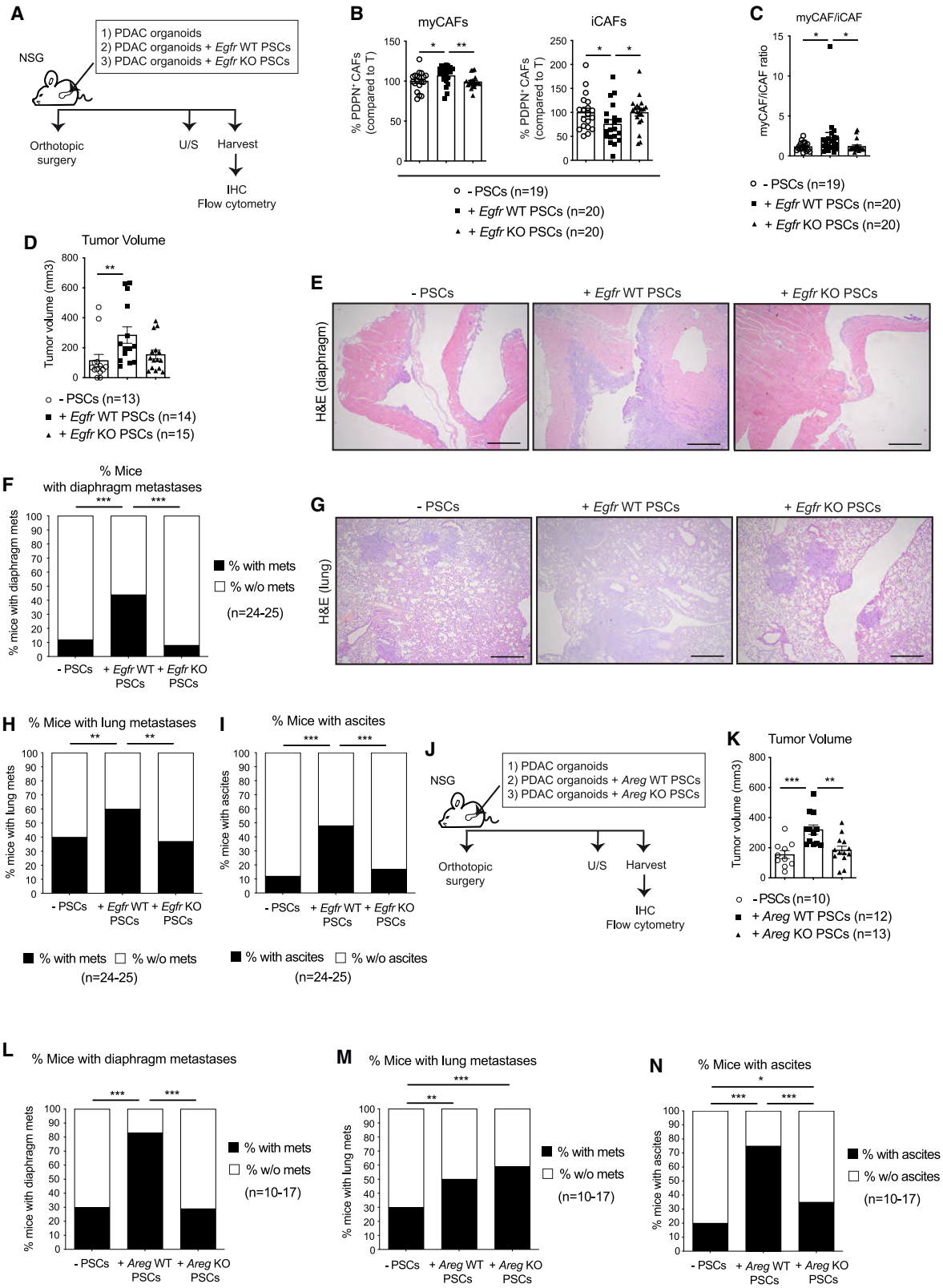

Figure 6. EGFR-activated myCAFs promote metastasis of PDAC

(A) Schematic of experimental design of models in NOD scid gamma (NSG) mice derived by the transplantation of PDAC organoids with or without *Egfr* WT (i.e., *Rosa26* KO) or *Egfr* KO PSCs.

(legend continued on next page)

in the PDAC dataset (Figure S2B), GSVA analysis of TCGA breast cancer BRCA dataset showed a positive correlation between a previously defined myCAF signature,[29] pathways known to be activated in myofibroblastic CAFs, such as TGF-β and HH signaling, and EGFR activation (Figure S7E). Additionally, similar to what we found in TCGA PAAD dataset, analysis of TCGA BRCA and lung cancer LUAD datasets showed a positive correlation between *TGFB1* expression and expression of *AREG*, as well as expression of myCAF markers (Figures S7F and S7G). Finally, TGF-β treatment induced *Areg* and *Dusp6* expression and activated EGFR signaling in mouse pulmonary fibroblasts (Figures S7H–S7J).

Together, these analyses suggest that EGFR activation occurs also in TGF-β-dependent myCAF populations of other malignancies and could be directly affected by EGFR/ERBB2-targeting strategies, as we showed in PDAC models.

DISCUSSION

With complementary *in vitro* and *in vivo* analyses, we reveal a previously unknown role for EGFR activation in a population of PDAC CAFs. Our data show that TGF-β induces AREG expression in PDAC myCAFs, triggering an autocrine EGFR/ERBB2 response. This network appears to fine-tune the balance of CAF cell states, favoring a myCAF relative to an iCAF phenotype. Accordingly, EGFR/ERBB2 inhibition preferentially targets myCAFs over iCAFs. Moreover, *in vivo*, this effect appears to be restricted to a subset of $CD90^{-}$ myCAFs that shows higher EGFR signaling activation. Finally, we demonstrate a role of EGFR-activated myCAFs in promoting PDAC metastasis in mice. We thereby unmask a mechanism by which bi-directional malignant cell-fibroblast crosstalk regulates PDAC myCAF molecular and functional heterogeneity and drives metastasis.

Phospho-EGFR has been previously detected in non-malignant cells in a $Kras^{G12D}$; $Egfr^{KO}$ mouse model of PDAC,[24] and AREG has been previously shown to promote sustained EGFR activation in homeostasis and inflammation.[30–32] Our work supports a role for CAF autocrine AREG signaling in sustaining EGFR activation in TGF-β-induced myCAFs. However, *Areg* deletion in CAFs does neither completely blunt phospho-EGFR levels *in vitro* nor blocks PDAC metastasis formation *in vivo* as effectively as *Egfr* deletion in CAFs. Together, these observations suggest that other autocrine and/or paracrine mediators contribute to sustained EGFR activation in myCAFs. Moreover, AREG secreted by malignant cells and/or immune cells, including macrophages,[33,34] may contribute to further boosting EGFR/ERBB2 activation in myCAFs. For example, it has been demonstrated that regulatory T cell (Treg) depletion leads to loss of myCAFs in PDAC.[35] Although this is likely dependent on Treg-produced TGF-β, Tregs also produce AREG,[36] whose reduction upon Treg depletion may also be involved in the observed reduction in myCAFs. However, the finding that AREG alone does not activate EGFR in PSCs suggests that while external sources of AREG may contribute to boosting EGFR signaling in PDAC myCAFs, they are not sufficient to activate this pathway in the absence of TGF-β signaling. Together, this corroborates a model in which activation of the TGF-β pathway is required for downstream AREG induction and effective EGFR signaling activation. Finally, our study shows that both EGFR and ERBB2 are activated in PSCs by TGF-β or PDAC organoid CM treatment, that EGFR/ERBB2 inhibition more profoundly downregulates *Areg* in myCAFs than EGFR inhibition alone, and that *Erbb2* deletion impairs EGFR activation. Thus, EGFR and ERBB2 appear to cooperate to induce *Areg* expression and activate downstream signaling in TGF-β-induced myCAFs.

Since EGFR/ERBB2 blockade downregulates *Areg* expression, this suggests a positive feedback loop within this

(B) Flow cytometric analyses of myCAFs ($CD45^{-}CD31^{-}EpCAM^{-}PDPN^{+}Ly6C^{-}$) and iCAFs ($CD45^{-}CD31^{-}EpCAM^{-}PDPN^{+}Ly6C^{+}$) from the $PDPN^{+}$ gate in tumors derived from the transplantation of PDAC organoids with or without *Egfr* WT or *Egfr* KO PSCs. Results from 4 separate experiments (n = 4–5 mice/cohort/experiment). PDAC+*Egfr* WT PSC tumors and PDAC+*Egfr* KO PSC tumors were compared to the PDAC alone tumors (T) of each individual experiment. This is needed to evaluate the effect of *Egfr* deletion on CAF composition across co-transplantation experiments performed with different PDAC organoid and PSC lines that generate tumors with various degrees of CAF composition and abundance.

(C) Flow cytometric analyses of myCAF/iCAF ratio from the $PDPN^{+}$ CAF gate in tumors derived from the transplantation of PDAC organoids with or without *Egfr* WT or *Egfr* KO PSCs. n = 19–20/cohort.

(D) Tumor volumes as measured by ultrasound of tumors derived from the transplantation of PDAC organoids with or without *Egfr* WT or *Egfr* KO PSCs. Results from 3 separate experiments (n = 3–5 mice/cohort/experiment).

(E) Representative hematoxylin and eosin (H&E) stains of diaphragm tissues (with metastases) from mice transplanted with PDAC organoids with or without *Egfr* WT or *Egfr* KO PSCs. Scale bars, 200 μm.

(F) Percentages of mice with or without diaphragm metastases in cohorts transplanted with PDAC organoids with or without *Egfr* WT or *Egfr* KO PSCs from 5 separate experiments (n = 4–5 mice/cohort/experiment).

(G) Representative H&E stains of lung tissues (with metastases) from mice transplanted with PDAC organoids with or without *Egfr* WT or *Egfr* KO PSCs. Scale bars, 200 μm.

(H) Percentages of mice with lung metastases in cohorts transplanted with PDAC organoids with or without *Egfr* WT or *Egfr* KO PSCs from 5 separate experiments (n = 4–5 mice/cohort/experiment).

(I) Percentages of mice with or without ascites in cohorts transplanted with PDAC organoids with or without *Egfr* WT or *Egfr* KO PSCs from 5 separate experiments (n = 4–5 mice/cohort/experiment).

(J) Schematic of experimental design of models in NSG mice derived by the transplantation of PDAC organoids with or without *Areg* WT (i.e., *Rosa26* KO) or *Areg* KO (i.e., 3 *Areg* KO clones from 2 different guide RNAs) PSCs.

(K) Tumor volumes as measured by ultrasound of tumors derived from the transplantation of PDAC organoids with or without *Areg* WT or *Areg* KO PSCs. Results from 10 to 13 mice from 2 separate experiments (n = 5–8 mice/cohort/experiment).

(L–N) Percentages of mice with or without diaphragm metastases (L), lung metastasis (M), or ascites in cohorts transplanted with PDAC organoids with or without *Areg* WT or *Areg* KO PSCs from 2 separate experiments (n = 10–17 mice). (B, C, D, and K) Results show mean ± SEM, Mann-Whitney test. (F, H, I, L, M, and N) Chi-square test. *, $p < 0.05$, **, $p < 0.01$; ***, $p < 0.001$. See also Figure S6.

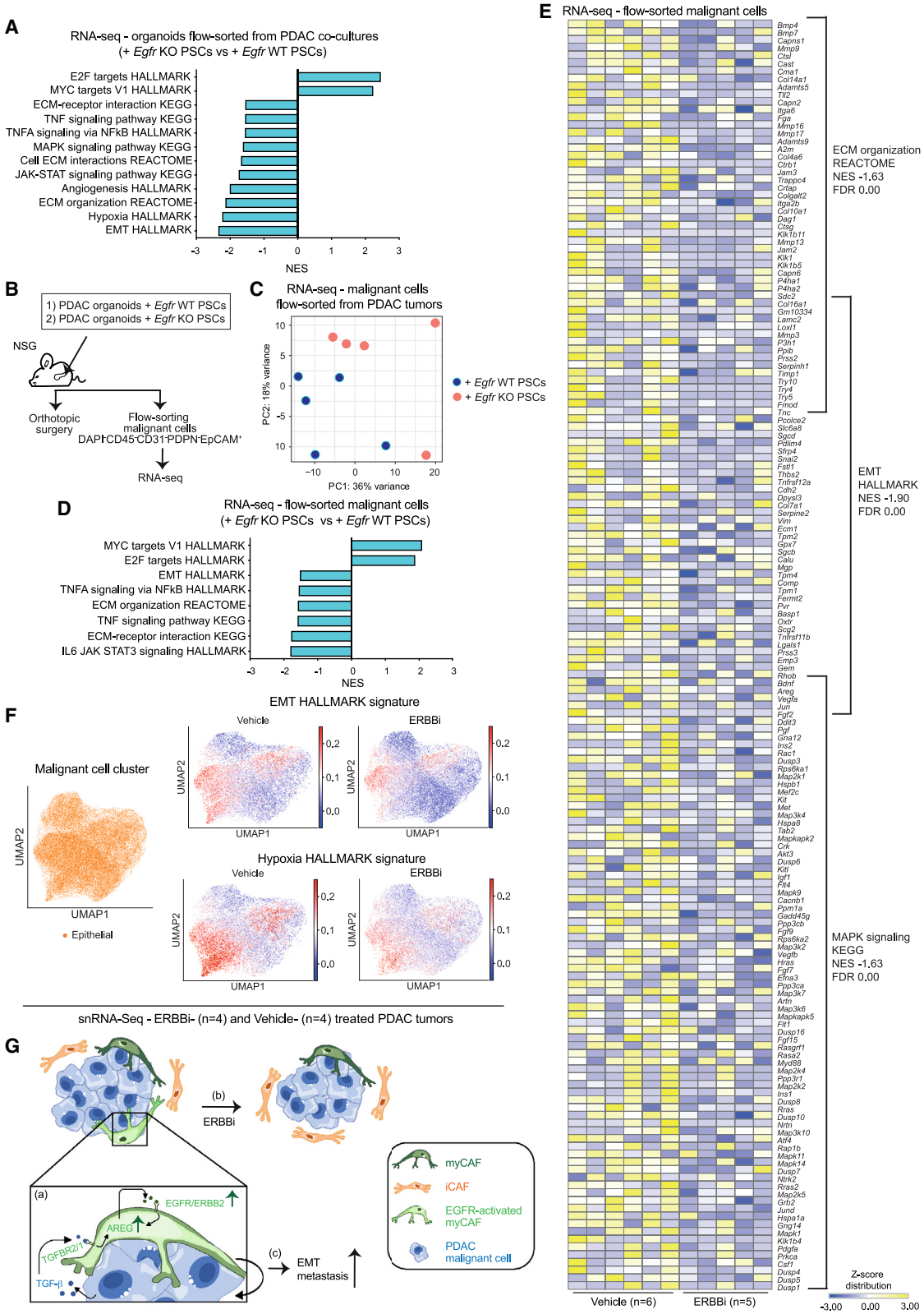

Figure 7. EGFR-activated myCAFs promote the metastatic potential of PDAC malignant cells

(A) Selected pathways found significantly enriched or depleted (NES > 1.5 or < −1.5; FDR < 0.25) by GSEA in malignant cells flow-sorted from co-cultures with *Egfr* KO PSCs (n = 7) compared to malignant cells flow-sorted from co-cultures with *Egfr* WT PSCs (n = 4).

(legend continued on next page)

ligand/receptor network. The observation that EGFR/ERBB2 inhibition downregulates *Areg* expression without affecting the TGF-β pathway suggests that this feedback is at the level of AREG, not at the level of TGF-β receptor activation. Indeed, previous studies showed that *Areg* is a gene target of EGFR signaling in fibroblasts and other cell types.[37,38] Dissecting the direct or indirect mechanism through which EGFR/ERBB2 signaling regulates *Areg* expression in TGF-β-induced myCAFs will require further work.

While we identified a tumor-promoting role of EGFR-activated myCAFs, previous work proposed a tumor-restraining role of αSMA-positive or HH-activated myofibroblasts,[13,15,21] largely attributing this to myCAF-mediated collagen deposition. Here we show that EGFR-activated CD90$^-$ myCAFs express lower collagen levels compared to CD90$^+$ myCAFs and that, as a result, EGFR/ERBB2 inhibition does not impact collagen abundance or overall fibrosis. Together, these observations highlight a previously unappreciated complexity of myCAF populations in PDAC and the need to further understand their molecular and functional heterogeneity to develop effective combinatorial strategies. Since non-myofibroblastic CAFs can also be tumor-promoting,[4] comparison of CD90$^-$ myCAFs not only to CD90$^+$ myCAFs, as in our study, but also to iCAF and apCAF populations will further unravel PDAC CAF biology.

CAFs have been shown to promote metastasis through various mechanisms. They can drive malignant cell aggressiveness by secreting proteins,[39–42] increase their viability and provide early growth advantage at secondary sites by co-migrating with them,[43,44] or exert force to drive malignant cell collective migration and invasiveness.[45–47] Our results suggest that genetic deletion or pharmacological inhibition of EGFR signaling in myCAFs impair the metastatic potential of malignant cells by downregulating the EMT signature, which has been shown to promote PDAC malignant cell plasticity and metastasis in some contexts.[25,26] While our analysis of CD90$^-$ myCAFs identified secreted proteins that could mediate this process, these EGFR-activated myCAFs may also have a rewired metabolism due to the increased expression of cholesterol biosynthesis-associated pathways. Rewiring of CAF metabolism has been shown to promote PDAC and we previously showed that cholesterol metabolism promotes PDAC aggressiveness.[48–50] Furthermore, hypoxia was shown to be involved in metastasis formation,[27] and the hypoxia gene signature was downregulated in PDAC malignant cells co-cultured with *Egfr* KO PSCs or isolated from ERBBi-treated tumors. Thus, EGFR-activated CAFs could boost PDAC aggressiveness in various ways. Further work will be required to fully dissect the mediators and mechanisms behind the promotion of PDAC metastasis by EGFR-activated myCAFs *in vivo* and will benefit from the generation of new fibroblast-specific genetically engineered mouse models (GEMMs).

We show that an EGFR/ERBB2 signaling network contributes to CAF heterogeneity and several CAF populations have been implicated in the regulation of the immune microenvironment.[4,8,12,51] While certain immune cell populations, including neutrophils and macrophages, were not affected by EGFR/ERBB2 inhibition, we observed an increase in T cell abundance in neratinib-treated PDAC tumors, in agreement with published data on EGFR inhibition.[20] Indeed, combination of erlotinib with immunotherapy has shown promising results in mouse models of PDAC.[20] Further work will be required to evaluate potential direct immunomodulatory effects of EGFR-activated myCAFs and to fully understand how these processes operate to drive PDAC progression.

As recent studies suggest that EGFR inhibition in PDAC may be helpful in combination with immunotherapies,[20] benefit *EGFR* WT cases[52] and revert resistance to KRAS inhibitors,[53] our study could be clinically relevant for PDAC patients. Additionally, our observations could have a broader impact, as our analyses suggest that activation of EGFR signaling also occurs in myofibroblasts of breast cancer and lung cancer, in which the EGFR/ERBB2 pathway is more commonly targeted in the clinic. Similarly, previous work has implicated EGFR activation and AREG upregulation in myofibroblasts in liver and pulmonary fibrosis.[54–57] Therefore, AREG/EGFR signaling may be common to numerous fibrotic diseases in which myofibroblasts play major roles.

Altogether, our study reveals EGFR/ERBB2 signaling as a pathway active in a subset of PDAC myCAFs, highlights previously unappreciated effects of EGFR/ERBB2 signaling inhibition on the PDAC stroma, which may also operate in other malignancies, and identifies a role for EGFR-activated myCAFs in promoting PDAC metastasis.

Limitations of the study

Co-transplantation of PDAC organoids with *Egfr* WT or *Egfr* KO PSCs requires to be performed in immunocompromised mice as co-injected PSCs need to be immortalized to survive *in vivo* over several weeks. Therefore, any potential direct effect of EGFR-activated CAFs on PDAC adaptive immunity remains to be investigated. Similarly, specific reprogramming of *Egfr*-deleted CAFs *in vivo* and functional validation of metastasis-promoting mediators produced by EGFR-activated CAFs will require further work. Efforts to address these open questions will benefit from the generation of new fibroblast-specific GEMMs.

(B) Schematic of experimental design of models in NSG mice derived by the transplantation of PDAC organoids with *Egfr* WT or *Egfr* KO PSCs for RNA-seq of flow-sorted malignant cells.
(C) PCA of malignant cells flow-sorted from PDAC tumors PDAC organoid-derived co-transplantation mouse models, as described in (B).
(D) Selected pathways found significantly enriched or depleted (NES > 1.5 or < −1.5; FDR < 0.25) by GSEA in malignant cells flow-sorted from PDAC organoid-derived co-transplantation mouse models with *Egfr* KO PSCs (n = 5) compared to PDAC organoid-derived co-transplantation mouse models with *Egfr* WT PSCs (n = 5).
(E) RNA-seq analysis of malignant cells flow-sorted from ERBBi-treated (n = 5) or vehicle-treated (n = 6) PDAC tumors from (D).
(F) UMAP plot of malignant/epithelial cells from ERBBi- (n = 4) or vehicle- (n = 4) treated PDAC tumors analyzed by snRNA-seq (left panel) from (F), and UMAP plots of malignant cells colored by the normalized expression score of the EMT signature (top panels) and the hypoxia signature (bottom panels).
(G) Model summarizing how the EGFR/ERBB2 pathway is activated in TGF-β-induced myCAFs via autocrine AREG (a), the effect of EGFR/ERBB2 inhibition (ERBBi) on PDAC CAF composition (b), and the metastasis-promoting role of EGFR-activated myCAFs in PDAC (c). See also Figure S7 and Table S6.

STAR★METHODS

Detailed methods are provided in the online version of this paper and include the following:

- KEY RESOURCES TABLE
- RESOURCE AVAILABILITY
  - Lead contact
  - Materials availability
  - Data and code availability
- EXPERIMENTAL MODEL DETAILS
  - Animals
  - Cell lines
- METHOD DETAILS
  - Mouse studies
  - *In vitro* cell cultures and treatments
  - CRISPR/Cas9 knockout in pancreatic stellate cells
  - Receptor tyrosine kinase assays
  - Western blot analyses
  - ELISA assays
  - Proliferation assays
  - Immunohistochemical and histological analyses
  - RNA *in situ hybridization* analyses
  - Flow cytometry analyses
  - Flow-sorting of pancreatic ductal adenocarcinoma organoid/pancreatic stellate cell co-cultures
  - Flow-sorting of pancreatic ductal adenocarcinoma tumors
  - Reverse transcription quantitative polymerase chain reaction analyses
  - RNA-sequencing and single-cell RNA-sequencing analyses
  - Single-nuclei RNA-sequencing analyses
- QUANTIFICATION AND STATISTICAL ANALYSIS

SUPPLEMENTAL INFORMATION

Supplemental information can be found online at https://doi.org/10.1016/j.ccell.2023.12.002.

ACKNOWLEDGMENTS

The authors would like to thank the BRU, Genomics, Bioinformatics, Flow cytometry, Pre-genome editing, RICS and Histology core facilities at the Cancer Research UK Cambridge Institute (CRUK-CI), University of Cambridge. The authors would also like to thank Philip Howden and the Cambridge Genomic Services at the Department of Pathology, University of Cambridge. Additionally, the authors would like to thank Alecia-Jane Twigger (Cambridge Stem Cell Institute) and Kui Hua (CRUK-CI) for sharing their optimized single-nuclei isolation protocol. Finally, the authors would also like to thank the Gene Expression Omnibus (GEO) team for their high-quality support. This work was mainly supported by a Cancer Research UK (CRUK) institutional grant (A27463) and a UKRI Future Leaders Fellowship that also supported G.B., S.P.T, W.L, S.A., and J.S.M. G.B. is also recipient of a Pancreatic Cancer Research Fund grant and a US Department of Defense PCARP grant that supported G.M. and J.S.M., an NCI-CRUK Cancer Grand Challenge grant that supported M.J. and W.K.L., and a Pancreatic Cancer UK Future Leaders Academy grant that supported P.S.W.C. Moreover, J.A.H. was supported by a Harding Distinguished Postgraduate Programme PhD studentship (Cambridge Trust), and E.G.L. was supported by an MRC Doctoral Training Grant. The results shown here are in part based on data generated by the TCGA Research Network (http://www.cancer.gov/tcga).

AUTHOR CONTRIBUTIONS

G.M. and J.A.H. designed the experiments, conducted the experiments and wrote the paper. S.P.T, J.S.M., M.J., W.L., E.G.L., S.A., W.K.L., and P.S.W.C conducted the experiments. A.S. and A.P. helped with designing the RNA-seq and snRNA-seq experiments. A.A. helped with single-nuclei isolation. G.B. designed the experiments, supervised the study, conducted the experiments and wrote the paper.

DECLARATION OF INTERESTS

The authors declare no competing interests.

Received: December 5, 2022
Revised: October 10, 2023
Accepted: December 4, 2023
Published: December 28, 2023

REFERENCES

1. Siegel, R.L., Miller, K.D., Fuchs, H.E., and Jemal, A. (2021). Cancer Statistics, 2021. CA A Cancer J. Clin. *71*, 7–33.
2. Bernard, V., Semaan, A., Huang, J., San Lucas, F.A., Mulu, F.C., Stephens, B.M., Guerrero, P.A., Huang, Y., Zhao, J., Kamyabi, N., et al. (2019). Single-Cell Transcriptomics of Pancreatic Cancer Precursors Demonstrates Epithelial and Microenvironmental Heterogeneity as an Early Event in Neoplastic Progression. Clin. Cancer Res. *25*, 2194–2205.
3. Biffi, G., Oni, T.E., Spielman, B., Hao, Y., Elyada, E., Park, Y., Preall, J., and Tuveson, D.A. (2019). IL1-Induced JAK/STAT Signaling Is Antagonized by TGFbeta to Shape CAF Heterogeneity in Pancreatic Ductal Adenocarcinoma. Cancer Discov. *9*, 282–301.
4. Biffi, G., and Tuveson, D.A. (2021). Diversity and Biology of Cancer-Associated Fibroblasts. Physiol. Rev. *101*, 147–176.
5. Dominguez, C.X., Müller, S., Keerthivasan, S., Koeppen, H., Hung, J., Gierke, S., Breart, B., Foreman, O., Bainbridge, T.W., Castiglioni, A., et al. (2020). Single-Cell RNA Sequencing Reveals Stromal Evolution into LRRC15(+) Myofibroblasts as a Determinant of Patient Response to Cancer Immunotherapy. Cancer Discov. *10*, 232–253.
6. Elyada, E., Bolisetty, M., Laise, P., Flynn, W.F., Courtois, E.T., Burkhart, R.A., Teinor, J.A., Belleau, P., Biffi, G., Lucito, M.S., et al. (2019). Cross-species single-cell analysis of pancreatic ductal adenocarcinoma reveals antigen-presenting cancer-associated fibroblasts. Cancer Discov. *9*, 1102–1123. CD-19-0094.
7. Hosein, A.N., Huang, H., Wang, Z., Parmar, K., Du, W., Huang, J., Maitra, A., Olson, E., Verma, U., and Brekken, R.A. (2019). Cellular heterogeneity during mouse pancreatic ductal adenocarcinoma progression at single-cell resolution. JCI Insight *5*, e129212.
8. Hutton, C., Heider, F., Blanco-Gomez, A., Banyard, A., Kononov, A., Zhang, X., Karim, S., Paulus-Hock, V., Watt, D., Steele, N., et al. (2021). Single-cell analysis defines a pancreatic fibroblast lineage that supports anti-tumor immunity. Cancer Cell *39*, 1227–1244.e20.
9. Öhlund, D., Handly-Santana, A., Biffi, G., Elyada, E., Almeida, A.S., Ponz-Sarvise, M., Corbo, V., Oni, T.E., Hearn, S.A., Lee, E.J., et al. (2017). Distinct populations of inflammatory fibroblasts and myofibroblasts in pancreatic cancer. J. Exp. Med. *214*, 579–596.
10. Peng, J., Sun, B.F., Chen, C.Y., Zhou, J.Y., Chen, Y.S., Chen, H., Liu, L., Huang, D., Jiang, J., Cui, G.S., et al. (2019). Single-cell RNA-seq highlights intra-tumoral heterogeneity and malignant progression in pancreatic ductal adenocarcinoma. Cell Res. *29*, 725–738.
11. Huang, H., Wang, Z., Zhang, Y., Pradhan, R.N., Ganguly, D., Chandra, R., Murimwa, G., Wright, S., Gu, X., Maddipati, R., et al. (2022). Mesothelial cell-derived antigen-presenting cancer-associated fibroblasts induce expansion of regulatory T cells in pancreatic cancer. Cancer Cell *40*, 656–673.e7.
12. Krishnamurty, A.T., Shyer, J.A., Thai, M., Gandham, V., Buechler, M.B., Yang, Y.A., Pradhan, R.N., Wang, A.W., Sanchez, P.L., Qu, Y., et al.

(2022). LRRC15+ myofibroblasts dictate the stromal setpoint to suppress tumour immunity. Nature *611*, 148–154.

13. Rhim, A.D., Oberstein, P.E., Thomas, D.H., Mirek, E.T., Palermo, C.F., Sastra, S.A., Dekleva, E.N., Saunders, T., Becerra, C.P., Tattersall, I.W., et al. (2014). Stromal Elements Act to Restrain, Rather Than Support, Pancreatic Ductal Adenocarcinoma. Cancer Cell *25*, 735–747.
14. McAndrews, K.M., Chen, Y., Darpolor, J.K., Zheng, X., Yang, S., Carstens, J.L., Li, B., Wang, H., Miyake, T., Correa de Sampaio, P., et al. (2022). Identification of Functional Heterogeneity of Carcinoma-Associated Fibroblasts with Distinct IL6-Mediated Therapy Resistance in Pancreatic Cancer. Cancer Discov. *12*, 1580–1597.
15. Özdemir, B.C., Pentcheva-Hoang, T., Carstens, J.L., Zheng, X., Wu, C.-C., Simpson, T.R., Laklai, H., Sugimoto, H., Kahlert, C., Novitskiy, S.V., et al. (2014). Depletion of carcinoma-associated fibroblasts and fibrosis induces immunosuppression and accelerates pancreas cancer with reduced survival. Cancer Cell *25*, 719–734.
16. Helms, E.J., Berry, M.W., Chaw, R.C., DuFort, C.C., Sun, D., Onate, M.K., Oon, C., Bhattacharyya, S., Sanford-Crane, H., Horton, W., et al. (2022). Mesenchymal Lineage Heterogeneity Underlies Nonredundant Functions of Pancreatic Cancer-Associated Fibroblasts. Cancer Discov. *12*, 484–501.
17. Zhang, Z., Kobayashi, S., Borczuk, A.C., Leidner, R.S., Laframboise, T., Levine, A.D., and Halmos, B. (2010). Dual specificity phosphatase 6 (DUSP6) is an ETS-regulated negative feedback mediator of oncogenic ERK signaling in lung cancer cells. Carcinogenesis *31*, 577–586.
18. Steele, N.G., Biffi, G., Kemp, S.B., Zhang, Y., Drouillard, D., Syu, L., Hao, Y., Oni, T.E., Brosnan, E., Elyada, E., et al. (2021). Inhibition of Hedgehog Signaling Alters Fibroblast Composition in Pancreatic Cancer. Clin. Cancer Res. *27*, 2023–2037.
19. Schwoerer, S., Cimino, F.V., Ros, M., Tsanov, K.M., Ng, C., Lowe, S.W., Carmona-Fontaine, C., and Thompson, C.B. (2023). Hypoxia Potentiates the Inflammatory Fibroblast Phenotype Promoted by Pancreatic Cancer Cell-Derived Cytokines. Cancer Res. *83:1596-1610*.
20. Li, J., Yuan, S., Norgard, R.J., Yan, F., Sun, Y.H., Kim, I.K., Merrell, A.J., Sela, Y., Jiang, Y., Bhanu, N.V., et al. (2021). Epigenetic and Transcriptional Control of the Epidermal Growth Factor Receptor Regulates the Tumor Immune Microenvironment in Pancreatic Cancer. Cancer Discov. *11*, 736–753.
21. Chen, Y., Kim, J., Yang, S., Wang, H., Wu, C.-J., Sugimoto, H., LeBleu, V.S., and Kalluri, R. (2021). Type I collagen deletion in αSMA+ myofibroblasts augments immune suppression and accelerates progression of pancreatic cancer. Cancer Cell *39*, 548–565.e6.
22. Casazza, A., Finisguerra, V., Capparuccia, L., Camperi, A., Swiercz, J.M., Rizzolio, S., Rolny, C., Christensen, C., Bertotti, A., Sarotto, I., et al. (2010). Sema3E-Plexin D1 signaling drives human cancer cell invasiveness and metastatic spreading in mice. J. Clin. Invest. *120*, 2684–2698.
23. Nallasamy, P., Nimmakayala, R.K., Karmakar, S., Leon, F., Seshacharyulu, P., Lakshmanan, I., Rachagani, S., Mallya, K., Zhang, C., Ly, Q.P., et al. (2021). Pancreatic Tumor Microenvironment Factor Promotes Cancer Stemness via SPP1–CD44 Axis. Gastroenterology *161*, 1998–2013.e7.
24. Ardito, C.M., Grüner, B.M., Takeuchi, K.K., Lubeseder-Martellato, C., Teichmann, N., Mazur, P.K., Delgiorno, K.E., Carpenter, E.S., Halbrook, C.J., Hall, J.C., et al. (2012). EGF receptor is required for KRAS-induced pancreatic tumorigenesis. Cancer Cell *22*, 304–317.
25. Aiello, N.M., Maddipati, R., Norgard, R.J., Balli, D., Li, J., Yuan, S., Yamazoe, T., Black, T., Sahmoud, A., Furth, E.E., et al. (2018). EMT Subtype Influences Epithelial Plasticity and Mode of Cell Migration. Dev. Cell *45*, 681–695.e4.
26. Krebs, A.M., Mitschke, J., Lasierra Losada, M., Schmalhofer, O., Boerries, M., Busch, H., Boettcher, M., Mougiakakos, D., Reichardt, W., Bronsert, P., et al. (2017). The EMT-activator Zeb1 is a key factor for cell plasticity and promotes metastasis in pancreatic cancer. Nat. Cell Biol. *19*, 518–529.
27. Rankin, E.B., Nam, J.-M., and Giaccia, A.J. (2016). Hypoxia: Signaling the Metastatic Cascade. Trends Cancer *2*, 295–304.
28. Geyer, C.E., Forster, J., Lindquist, D., Chan, S., Romieu, C.G., Pienkowski, T., Jagiello-Gruszfeld, A., Crown, J., Chan, A., Kaufman, B., et al. (2006). Lapatinib plus capecitabine for HER2-positive advanced breast cancer. N. Engl. J. Med. *355*, 2733–2743.
29. Bartoschek, M., Oskolkov, N., Bocci, M., Lövrot, J., Larsson, C., Sommarin, M., Madsen, C.D., Lindgren, D., Pekar, G., Karlsson, G., et al. (2018). Spatially and functionally distinct subclasses of breast cancer-associated fibroblasts revealed by single cell RNA sequencing. Nat. Commun. *9*, 5150.
30. Roepstorff, K., Grandal, M.V., Henriksen, L., Knudsen, S.L.J., Lerdrup, M., Grøvdal, L., Willumsen, B.M., and van Deurs, B. (2009). Differential effects of EGFR ligands on endocytic sorting of the receptor. Traffic *10*, 1115–1127.
31. Stern, K.A., Place, T.L., and Lill, N.L. (2008). EGF and amphiregulin differentially regulate Cbl recruitment to endosomes and EGF receptor fate. Biochem. J. *410*, 585–594.
32. Zaiss, D.M.W., Gause, W.C., Osborne, L.C., and Artis, D. (2015). Emerging functions of amphiregulin in orchestrating immunity, inflammation, and tissue repair. Immunity *42*, 216–226.
33. Minutti, C.M., Modak, R.V., Macdonald, F., Li, F., Smyth, D.J., Dorward, D.A., Blair, N., Husovsky, C., Muir, A., Giampazolias, E., et al. (2019). A Macrophage-Pericyte Axis Directs Tissue Restoration via Amphiregulin-Induced Transforming Growth Factor Beta Activation. Immunity *50*, 645–654.e6.
34. Buechler, M.B., Fu, W., and Turley, S.J. (2021). Fibroblast-macrophage reciprocal interactions in health, fibrosis, and cancer. Immunity *54*, 903–915.
35. Zhang, Y., Lazarus, J., Steele, N.G., Yan, W., Lee, H.J., Nwosu, Z.C., Halbrook, C.J., Menjivar, R.E., Kemp, S.B., Sirihorachai, V.R., et al. (2020). Regulatory T-cell Depletion Alters the Tumor Microenvironment and Accelerates Pancreatic Carcinogenesis. Cancer Discov. *10*, 422–439.
36. Arpaia, N., Green, J.A., Moltedo, B., Arvey, A., Hemmers, S., Yuan, S., Treuting, P.M., and Rudensky, A.Y. (2015). A Distinct Function of Regulatory T Cells in Tissue Protection. Cell *162*, 1078–1089.
37. Panupinthu, N., Yu, S., Zhang, D., Zhang, F., Gagea, M., Lu, Y., Grandis, J.R., Dunn, S.E., Lee, H.Y., and Mills, G.B. (2014). Self-reinforcing loop of amphiregulin and Y-box binding protein-1 contributes to poor outcomes in ovarian cancer. Oncogene *33*, 2846–2856.
38. Inatomi, O., Andoh, A., Yagi, Y., Bamba, S., Tsujikawa, T., and Fujiyama, Y. (2006). Regulation of amphiregulin and epiregulin expression in human colonic subepithelial myofibroblasts. Int. J. Mol. Med. *18*, 497–503.
39. Calon, A., Espinet, E., Palomo-Ponce, S., Tauriello, D.V.F., Iglesias, M., Céspedes, M.V., Sevillano, M., Nadal, C., Jung, P., Zhang, X.H.-F., et al. (2012). Dependency of Colorectal Cancer on a TGF-β-Driven Program in Stromal Cells for Metastasis Initiation. Cancer Cell *22*, 571–584.
40. Waghray, M., Yalamanchili, M., Dziubinski, M., Zeinali, M., Erkkinen, M., Yang, H., Schradle, K.A., Urs, S., Pasca Di Magliano, M., Welling, T.H., et al. (2016). GM-CSF Mediates Mesenchymal–Epithelial Cross-talk in Pancreatic Cancer. Cancer Discov. *6*, 886–899.
41. Grugan, K.D., Miller, C.G., Yao, Y., Michaylira, C.Z., Ohashi, S., Klein-Szanto, A.J., Diehl, J.A., Herlyn, M., Han, M., Nakagawa, H., and Rustgi, A.K. (2010). Fibroblast-secreted hepatocyte growth factor plays a functional role in esophageal squamous cell carcinoma invasion. Proc. Natl. Acad. Sci. USA *107*, 11026–11031.
42. Djurec, M., Graña, O., Lee, A., Troulé, K., Espinet, E., Cabras, L., Navas, C., Blasco, M.T., Martín-Díaz, L., Burdiel, M., et al. (2018). Saa3 is a key mediator of the protumorigenic properties of cancer-associated fibroblasts in pancreatic tumors. Proc. Natl. Acad. Sci. USA *115*, E1147–E1156.
43. Duda, D.G., Duyverman, A.M.M.J., Kohno, M., Snuderl, M., Steller, E.J.A., Fukumura, D., and Jain, R.K. (2010). Malignant cells facilitate lung metastasis by bringing their own soil. Proc. Natl. Acad. Sci. USA *107*, 21677–21682.

44. Ao, Z., Shah, S.H., Machlin, L.M., Parajuli, R., Miller, P.C., Rawal, S., Williams, A.J., Cote, R.J., Lippman, M.E., Datar, R.H., and El-Ashry, D. (2015). Identification of Cancer-Associated Fibroblasts in Circulating Blood from Patients with Metastatic Breast Cancer. Cancer Res. *75*, 4681–4687.

45. Gaggioli, C., Hooper, S., Hidalgo-Carcedo, C., Grosse, R., Marshall, J.F., Harrington, K., and Sahai, E. (2007). Fibroblast-led collective invasion of carcinoma cells with differing roles for RhoGTPases in leading and following cells. Nat. Cell Biol. *9*, 1392–1400.

46. Goetz, J.G., Minguet, S., Navarro-Lérida, I., Lazcano, J.J., Samaniego, R., Calvo, E., Tello, M., Osteso-Ibáñez, T., Pellinen, T., Echarri, A., et al. (2011). Biomechanical Remodeling of the Microenvironment by Stromal Caveolin-1 Favors Tumor Invasion and Metastasis. Cell *146*, 148–163.

47. Labernadie, A., Kato, T., Brugués, A., Serra-Picamal, X., Derzsi, S., Arwert, E., Weston, A., González-Tarragó, V., Elosegui-Artola, A., Albertazzi, L., et al. (2017). A mechanically active heterotypic E-cadherin/N-cadherin adhesion enables fibroblasts to drive cancer cell invasion. Nat. Cell Biol. *19*, 224–237.

48. Oni, T.E., Biffi, G., Baker, L.A., Hao, Y., Tonelli, C., Somerville, T.D.D., Deschênes, A., Belleau, P., Hwang, C.I., Sánchez-Rivera, F.J., et al. (2020). SOAT1 promotes mevalonate pathway dependency in pancreatic cancer. J. Exp. Med. *217*, e20192389.

49. Auciello, F.R., Bulusu, V., Oon, C., Tait-Mulder, J., Berry, M., Bhattacharyya, S., Tumanov, S., Allen-Petersen, B.L., Link, J., Kendsersky, N.D., et al. (2019). A Stromal Lysolipid–Autotaxin Signaling Axis Promotes Pancreatic Tumor Progression. Cancer Discov. *9*, 617–627.

50. Sousa, C.M., Biancur, D.E., Wang, X., Halbrook, C.J., Sherman, M.H., Zhang, L., Kremer, D., Hwang, R.F., Witkiewicz, A.K., Ying, H., et al. (2016). Pancreatic stellate cells support tumour metabolism through autophagic alanine secretion. Nature *536*, 479–483.

51. Feig, C., Jones, J.O., Kraman, M., Wells, R.J.B., Deonarine, A., Chan, D.S., Connell, C.M., Roberts, E.W., Zhao, Q., Caballero, O.L., et al. (2013). Targeting CXCL12 from FAP-expressing carcinoma-associated fibroblasts synergizes with anti–PD-L1 immunotherapy in pancreatic cancer. Proc. Natl. Acad. Sci. USA *110*, 20212–20217.

52. Boeck, S., Jung, A., Laubender, R.P., Neumann, J., Egg, R., Goritschan, C., Vehling-Kaiser, U., Winkelmann, C., Fischer von Weikersthal, L., Clemens, M.R., et al. (2013). EGFR pathway biomarkers in erlotinib-treated patients with advanced pancreatic cancer: translational results from the randomised, crossover phase 3 trial AIO-PK0104. Br. J. Cancer *108*, 469–476.

53. Amodio, V., Yaeger, R., Arcella, P., Cancelliere, C., Lamba, S., Lorenzato, A., Arena, S., Montone, M., Mussolin, B., Bian, Y., et al. (2020). EGFR Blockade Reverts Resistance to KRAS(G12C) Inhibition in Colorectal Cancer. Cancer Discov. *10*, 1129–1139.

54. Fuchs, B.C., Hoshida, Y., Fujii, T., Wei, L., Yamada, S., Lauwers, G.Y., McGinn, C.M., DePeralta, D.K., Chen, X., Kuroda, T., et al. (2014). Epidermal growth factor receptor inhibition attenuates liver fibrosis and development of hepatocellular carcinoma. Hepatology *59*, 1577–1590.

55. Perugorria, M.J., Latasa, M.U., Nicou, A., Cartagena-Lirola, H., Castillo, J., Goñi, S., Vespasiani-Gentilucci, U., Zagami, M.G., Lotersztajn, S., Prieto, J., et al. (2008). The epidermal growth factor receptor ligand amphiregulin participates in the development of mouse liver fibrosis. Hepatology *48*, 1251–1261.

56. Xu, H., Liu, L., Cong, M., Liu, T., Sun, S., Ma, H., You, H., Jia, J., and Wang, P. (2020). EGF neutralization antibodies attenuate liver fibrosis by inhibiting myofibroblast proliferation in bile duct ligation mice. Histochem. Cell Biol. *154*, 107–116.

57. Zhou, Y., Lee, J.Y., Lee, C.M., Cho, W.K., Kang, M.J., Koff, J.L., Yoon, P.O., Chae, J., Park, H.O., Elias, J.A., and Lee, C.G. (2012). Amphiregulin, an epidermal growth factor receptor ligand, plays an essential role in the pathogenesis of transforming growth factor-beta-induced pulmonary fibrosis. J. Biol. Chem. *287*, 41991–42000.

58. Boj, S.F., Hwang, C.-I., Baker, L.A., Chio, I.I.C., Engle, D.D., Corbo, V., Jager, M., Ponz-Sarvise, M., Tiriac, H., Spector, M.S., et al. (2015). Organoid models of human and mouse ductal pancreatic cancer. Cell *160*, 324–338.

59. Sanjana, N.E., Shalem, O., and Zhang, F. (2014). Improved vectors and genome-wide libraries for CRISPR screening. Nat. Methods *11*, 783–784.

60. Roe, J.-S., Hwang, C.-I., Somerville, T.D.D., Milazzo, J.P., Lee, E.J., Da Silva, B., Maiorino, L., Tiriac, H., Young, C.M., Miyabayashi, K., et al. (2017). Enhancer Reprogramming Promotes Pancreatic Cancer Metastasis. Cell *170*, 875–888.e20.

61. Schneider, C.A., Rasband, W.S., and Eliceiri, K.W. (2012). NIH Image to ImageJ: 25 years of image analysis. Nat. Methods *9*, 671–675.

62. Patro, R., Duggal, G., Love, M.I., Irizarry, R.A., and Kingsford, C. (2017). Salmon provides fast and bias-aware quantification of transcript expression. Nat. Methods *14*, 417–419.

63. Soneson, C., Love, M.I., and Robinson, M.D. (2015). Differential analyses for RNA-seq: transcript-level estimates improve gene-level inferences. F1000Res. *4*, 1521.

64. Love, M.I., Huber, W., and Anders, S. (2014). Moderated estimation of fold change and dispersion for RNA-seq data with DESeq2. Genome Biol. *15*, 550.

65. Wu, T., Hu, E., Xu, S., Chen, M., Guo, P., Dai, Z., Feng, T., Zhou, L., Tang, W., Zhan, L., et al. (2021). clusterProfiler 4.0: A universal enrichment tool for interpreting omics data. Innovation *2*, 100141.

66. Castanza, A.S., Recla, J.M., Eby, D., Thorvaldsdóttir, H., Bult, C.J., and Mesirov, J.P. (2023). Extending support for mouse data in the Molecular Signatures Database (MSigDB). Nat. Methods *20*, 1619–1620.

67. Subramanian, A., Tamayo, P., Mootha, V.K., Mukherjee, S., Ebert, B.L., Gillette, M.A., Paulovich, A., Pomeroy, S.L., Golub, T.R., Lander, E.S., and Mesirov, J.P. (2005). Gene set enrichment analysis: A knowledge-based approach for interpreting genome-wide expression profiles. Proc. Natl. Acad. Sci. USA *102*, 15545–15550.

68. Hänzelmann, S., Castelo, R., and Guinney, J. (2013). GSVA: gene set variation analysis for microarray and RNA-seq data. BMC Bioinf. *14*, 7.

69. Fleming, S.J., Chaffin, M.D., Arduini, A., Akkad, A.-D., Banks, E., Marioni, J.C., Philippakis, A.A., Ellinor, P.T., and Babadi, M. (2023). Unsupervised removal of systematic background noise from droplet-based single-cell experiments using CellBender. Nat. Methods *20*, 1323–1335.

70. Bernstein, N.J., Fong, N.L., Lam, I., Roy, M.A., Hendrickson, D.G., and Kelley, D.R. (2020). Solo: Doublet Identification in Single-Cell RNA-Seq via Semi-Supervised Deep Learning. Cell Syst. *11*, 95–101.e5.

71. Korsunsky, I., Millard, N., Fan, J., Slowikowski, K., Zhang, F., Wei, K., Baglaenko, Y., Brenner, M., Loh, P.R., and Raychaudhuri, S. (2019). Fast, sensitive and accurate integration of single-cell data with Harmony. Nat. Methods *16*, 1289–1296.

72. Wolf, F.A., Angerer, P., and Theis, F.J. (2018). SCANPY: large-scale single-cell gene expression data analysis. Genome Biol. *19*, 15.

73. Traag, V.A., Waltman, L., and van Eck, N.J. (2019). From Louvain to Leiden: guaranteeing well-connected communities. Sci. Rep. *9*, 5233.

74. Finak, G., McDavid, A., Yajima, M., Deng, J., Gersuk, V., Shalek, A.K., Slichter, C.K., Miller, H.W., McElrath, M.J., Prlic, M., et al. (2015). MAST: a flexible statistical framework for assessing transcriptional changes and characterizing heterogeneity in single-cell RNA sequencing data. Genome Biol. *16*, 278.

STAR★METHODS

KEY RESOURCES TABLE

REAGENT or RESOURCE	SOURCE	IDENTIFIER
Antibodies		
Rabbit polyclonal anti-HSP90α	Merck Millipore	Cat# 07-2174; RRID: AB_10807022
Rabbit monoclonal anti-pan-ACTIN (clone D18C11)	Cell Signaling Technology	Cat# 8456; RRID: AB_10998774
Rabbit monoclonal anti-SMAD2 (clone D43B4)	Cell Signaling Technology	Cat# 5339; RRID: AB_10626777
Rabbit monoclonal anti-phospho-SMAD2/SMAD3 (clone D27F4)	Cell Signaling Technology	Cat# 8828; RRID: AB_2631089
Goat polyclonal anti-TGFBR2	R&D Systems	Cat# AF532; RRID: AB_355418
Rabbit monoclonal anti-ERBB2 (clone 29D8)	Cell Signaling Technology	Cat# 2165; RRID: AB_10692490
Rabbit polyclonal anti-phospho-ERBB2	Cell Signaling Technology	Cat# 2247; RRID: AB_331725
Rabbit monoclonal anti-EGFR (clone D38B1)	Cell Signaling Technology	Cat# 4267; RRID: AB_2246311
Rabbit monoclonal anti-phospho-EGFR (clone D7A5)	Cell Signaling Technology	Cat# 3777; RRID: AB_2096270
Rabbit monoclonal anti-CC3 (clone 5A1E)	Cell Signaling Technology	Cat# 9664; RRID: AB_2096270
Peroxidase AffiniPure Donkey Anti-Rabbit IgG (H + L)	Jackson ImmunoResearch	Cat# 711-035-152; RRID: AB_10015282
Peroxidase AffiniPure Donkey Anti-Goat IgG (H + L)	Jackson ImmunoResearch	Cat# 705-035-003; RRID: AB_2340390
Rabbit monoclonal anti-phospho-EGFR (clone EP774Y)	Abcam	Cat# ab40815; RRID: AB_732110
Rabbit polyclonal anti-αSMA	Abcam	Cat# ab5694; RRID: AB_2223021
Mouse monoclonal anti-SV40 large T antigen	Abcam	Cat# ab16879; RRID: AB 302561
Rat monoclonal anti-CD31-PE/Cy7 (clone 390)	BioLegend	Cat# 102418; RRID: AB_830757
Rat monoclonal anti-CD31-PerCP/Cy5.5 (clone 390)	BioLegend	Cat# 102419; RRID: AB_10612742
Rat monoclonal anti-CD45-PerCP/Cy5.5 (clone 30-F11)	BioLegend	Cat# 103132; RRID: AB_893340
Rat monoclonal anti-CD326 (EpCAM)-AlexaFluor 488 (clone G8.8)	BioLegend	Cat# 118210; RRID: AB_1134099
Rat monoclonal CD326 (EpCAM)-PE (clone G8.8)	BioLegend	Cat# 118205; RRID: AB_1134176
Rat monoclonal CD326 (EpCAM)-Alexa Fluor 647 (clone G8.8)	BioLegend	Cat# 118212; RRID: AB_1134104
Syrian Hamster monoclonal PDPN-APC/Cy7 (clone 8.1.1)	BioLegend	Cat# 127418; RRID: AB_2629804
Syrian Hamster monoclonal PDPN-AlexaFluor 488 (clone 8.1.1)	BioLegend	Cat# 127405; RRID: AB_1133992
Rat monoclonal MHCII-BV785 (clone M5/114.15.2)	BioLegend	Cat# 107645; RRID: AB_2565977
Rat monoclonal MHCII-APC/Cy7 (clone M5/114.15.2)	BioLegend	Cat# 107627; RRID: AB_1659252
Rat monoclonal Ly6C-APC (clone HK1.4)	BioLegend	Cat# 128015; RRID: AB_1732087
Rat monoclonal Ly6C-Alexa488 (clone HK1.4)	BioLegend	Cat# 128021; RRID: AB_10640820
Rat monoclonal CD90-PE (G7)	Abcam	Cat# ab24904; RRID: AB_448474
Armenian Hamster monoclonal TCR-β-Alexa488 (clone H57-597)	BioLegend	Cat# 109215; RRID: AB_493344
Armenian Hamster monoclonal CD3e-Alexa488 (clone 145-2C11)	BioLegend	Cat#100321; RRID: AB_389300
Rat monoclonal CD8-APC/Cy7 (clone 53–6.7)	BioLegend	Cat#100713; RRID: AB_312752
Rat monoclonal CD4-APC (clone RM4-5)	BioLegend	Cat#100515; RRID: AB_312718
Rat monoclonal CD11b-PE/Cy7 (clone M1/70)	BioLegend	Cat#101215; RRID: AB_312798
Rat monoclonal F4/80-BV785 (clone BM8)	BioLegend	Cat#123141; RRID: AB_2563667
Armenian Hamster monoclonal CD11c-APC (clone N418)	BioLegend	Cat#117309; RRID: AB_313778
Rat monoclonal Gr1-PE (clone RB6-8C5)	BioLegend	Cat# 108407; RRID: AB_313372
Chemicals, peptides, and recombinant proteins		
EGFR/ERBB2 inhibitor Neratinib	Selleckchem	Cat# S2150
EGFR/ERBB2 inhibitor Neratinib	MedChem Express	Cat# HY32721

(*Continued on next page*)

Continued

REAGENT or RESOURCE	SOURCE	IDENTIFIER
EGFR inhibitor Erlotinib HCl	Stratech Scientific Ltd	Cat# S1023-SEL
TGFBR1 inhibitor A83-01	Tocris Bioscience	Cat# 2939
Recombinant human TGF-β1	Sigma-Aldrich	Cat# T7039
Recombinant murine AREG	PeproTech	Cat# 315-36
Critical commercial assays		
Proteome profiler mouse phospho-RTK array kit	R&D Systems	Cat# ARY014
Murine AREG ELISA kit	Thermo Fisher Scientific	Cat# EMAREG
Murine TGF-β1 ELISA kit	Thermo Fisher Scientific	Cat# BMS608-4
CellTiter-Glo kit	Promega	Cat# G7572
RNA Scope colorimetric kit	Advanced Cell Diagnostics	Cat# 322360
Murine probe for *Areg* for RNA Scope	Advanced Cell Diagnostics	Cat# 430501
Hydrogen peroxide and protease Plus reagent for RNA Scope	Advanced Cell Diagnostics	Cat# 322330
ImmPRESS[R] HRP Horse Anti-Rabbit IgG Polymer Detection Kit, Peroxidase	Vector Laboratories	Cat# MP-7401-50
ImmPRESS[R] HRP Horse Anti-Mouse IgG Polymer Detection Kit, Peroxidase	Vector Laboratories	Cat# MP-7402-50
ImmPACT(R) DAB substrate kit	Vector Laboratories	Cat# VEC-SK-4105
TaqMan reverse transcription reagents	Applied Biosystems	Cat# N808-0234
TaqMan master mix	Applied Biosystems	Cat# 4440040
Murine TaqMan probe *Acta2* Mm01546133_m1	Thermo Fisher Scientific	https://www.thermofisher.com/taqman-gene-expression/product/Mm01546133_m1?CID = &ICID = &subtype =
Murine TaqMan probe *Areg* Mm01354339_m1	Thermo Fisher Scientific	https://www.thermofisher.com/order/genome-database/details/gene-expression/Mm01354339_m1
Murine TaqMan probe *Btc* Mm00432137_m1	Thermo Fisher Scientific	https://www.thermofisher.com/taqman-gene-expression/product/Mm00432137_m1?CID = &ICID = &subtype =
Murine TaqMan probe *Col1a1* Mm00801666_g1	Thermo Fisher Scientific	https://www.thermofisher.com/taqman-gene-expression/product/Mm00801666_g1?CID = &ICID = &subtype =
Murine TaqMan probe *Csf3* Mm00438334_m1	Thermo Fisher Scientific	https://www.thermofisher.com/taqman-gene-expression/product/Mm00438334_m1?CID = &ICID = &subtype =
Murine TaqMan probe *Ctgf* Mm01192932_g1	Thermo Fisher Scientific	https://www.thermofisher.com/taqman-gene-expression/product/Mm01192932_g1?CID = &ICID = &subtype =
Murine TaqMan probe *Cxcl1* Mm04207460_m1	Thermo Fisher Scientific	https://www.thermofisher.com/taqman-gene-expression/product/Mm04207460_m1?CID = &ICID = &subtype =
Murine TaqMan probe *Dusp6* Mm00518185_m1	Thermo Fisher Scientific	https://www.thermofisher.com/taqman-gene-expression/product/Mm00518185_m1?CID = &ICID = &subtype =
Murine TaqMan probe *Egf* Mm00438696_m1	Thermo Fisher Scientific	https://www.thermofisher.com/taqman-gene-expression/product/Mm00438696_m1?CID = &ICID = &subtype =
Murine TaqMan probe *Ereg* Mm00514794_m1	Thermo Fisher Scientific	https://www.thermofisher.com/taqman-gene-expression/product/Mm00514794_m1?CID = &ICID = &subtype =
Murine TaqMan probe *Hbegf* Mm00439306_m1	Thermo Fisher Scientific	https://www.thermofisher.com/taqman-gene-expression/product/Mm00439306_m1?CID = &ICID = &subtype =

(*Continued on next page*)

Continued

REAGENT or RESOURCE	SOURCE	IDENTIFIER
Murine TaqMan probe *Hprt* Mm00446968_m1	Thermo Fisher Scientific	https://www.thermofisher.com/taqman-gene-expression/product/Mm00446968_m1?CID = &ICID = &subtype =
Murine TaqMan probe *Il1a* Mm00439620_m1	Thermo Fisher Scientific	https://www.thermofisher.com/taqman-gene-expression/product/Mm00439620_m1?CID = &ICID = &subtype =
Murine TaqMan probe *Il6* Mm00446190_m1	Thermo Fisher Scientific	https://www.thermofisher.com/taqman-gene-expression/product/Mm00446190_m1?CID = &ICID = &subtype =
Murine TaqMan probe *Nrg1* Mm01212130_m1	Thermo Fisher Scientific	https://www.thermofisher.com/taqman-gene-expression/product/Mm01212130_m1?CID = &ICID = &subtype =
Murine TaqMan probe *Tgfa* Mm00446232_m1	Thermo Fisher Scientific	https://www.thermofisher.com/taqman-gene-expression/product/Mm00446232_m1?CID = &ICID = &subtype =
Murine TaqMan probe *Tgfb1* Mm01178820_m1	Thermo Fisher Scientific	https://www.thermofisher.com/taqman-gene-expression/product/Mm01178820_m1?CID = &ICID = &subtype =
PureLink RNA mini kit	Invitrogen	Cat#12183018A
RNeasy Micro kit	Qiagen	Cat#74004
Qubit RNA High Sensitivity kit	Thermo Fisher Scientific	Cat#Q32852
Qubit RNA Broad Range kit	Thermo Fisher Scientific	Cat#Q10210
Agilent RNA ScreenTape kit	Agilent Technologies	Cat#5067-5576
Agilent High sensitivity RNA ScreenTape kit	Agilent Technologies	Cat#5067-5579
Agilent RNA 6000 Nano kit	Agilent Technologies	Cat#5067-1511
Agilent RNA 6000 Pico kit	Agilent Technologies	Cat#5067-1513
Agilent High Sensitivity 5000 ScreenTape	Agilent Technologies	Cat#5067-5588
Agilent High Sensitivity D1000 ScreenTape	Agilent Technologies	Cat#5067-5584
NEBNext Single Cell/Low Input RNA Library Prep Kit	New England Biolabs	Cat#E6420S
NEBNext Multiplex Oligos	New England Biolabs	Cat#E6440S
SMART-Seq Stranded Kit	Takara Bio	Cat#634442
Next GEM Single Cell 3′ Kit v3.1	Chromium	Cat#PN-1000268
Next GEM Chip G Single Cell Kit	Chromium	Cat#PN-1000120
Dual Index Kit TT Set A	Chromium	Cat#PN-1000215
Quant-iT dsDNA Assay Kit for high sensitivity	Invitrogen	Cat#Q33120
Deposited data		
Raw and analyzed RNA-sequencing and single-nuclei RNA-sequencing data	This paper	GEO: GSE243892
Mouse reference genome GRCm38 (release 102)	Genome Reference Consortium	http://nov2020.archive.ensembl.org/Mus_musculus/Info/Index
Mouse reference genome GRCh39 (mm39)	Genome Reference Consortium	https://www.ensembl.org/Mus_musculus/Info/Index
Human PDAC single-cell RNA-sequencing data	Elyada et al.[6]	NCBI dbGaP; accession number phs001840.v1.p1
Murine KPC PDAC single-cell RNA-sequencing data	Elyada et al.[6]	GEO: GSE129455
PAAD dataset	TCGA	http://firebrowse.org/?cohort=PAAD&download_dialogue=true
LUAD dataset	TCGA	http://firebrowse.org/?cohort = LUAD&download_dialogue = true
BRCA dataset	TCGA	http://firebrowse.org/?cohort = BRCA&download_dialogue = true
Murine breast cancer single-cell RNA-sequencing data (for myofibroblast signature)	Bartoschek et al.[29]	The myofibroblast signature was obtained from Table S1.

(*Continued on next page*)

Continued

REAGENT or RESOURCE	SOURCE	IDENTIFIER
Murine PDAC single-cell RNA-sequencing data (for LRRC15$^+$ CAF signature)	Dominguez et al.[5]	The LRRC15$^+$ CAF signature was obtained from Table S1.
Murine PDAC single-cell RNA-sequencing data (for cCAF3 signature)	McAndrews et al.[14]	The cCAF3 signature was obtained from Table S5.
Murine PDAC organoid RNA-sequencing data	Oni et al.[48]	GEO: GSE142467; GEO: GSE63348.
Experimental models: Cell lines		
Mouse: T69A PDAC organoids	Oni et al.[48]	N/A
Mouse: T6-LOH PDAC organoids	Oni et al.[48]	N/A
Mouse: T23-LOH PDAC organoids	Oni et al.[48]	N/A
Mouse: GB-T12-LOH PDAC organoids	This paper	N/A
Mouse: SV40-immortalized PSC4	Öhlund et al.[9]	N/A
Mouse: SV40-immortalized PSC5	Öhlund et al.[9]	N/A
Mouse: SV40-immortalized PSC23	This paper	N/A
Mouse: primary pulmonary fibroblasts	ScienCell	M3300-57
Mouse: SV40-immortalized pulmonary fibroblasts	This paper	N/A
Human: SV40-immortalized hPSCs	Biffi et al.[3]	N/A
Mouse: *Egfr* KO SV40-immortalized PSC4	This paper	Clones: 1.1 B4, 1.2 A3
Mouse: *Egfr* KO SV40-immortalized PSC5	This paper	Clones: 2.1 B4, 1.1 C5, 3.1 D4
Mouse: *Areg* KO SV40-immortalized PSC5	This paper	Clones: 2.2 E2, 2.2 E3, 1.1 G10
Mouse: *Tgfbr2* KO SV40-immortalized PSC4	This paper	Clones: 1.2 A3, 1.1 A10
Mouse: *Tgfbr2* KO SV40-immortalized PSC5	This paper	Clones: 1.3 B11, 1.2 D4, 1.1 E8
Mouse: *Rosa26* KO SV40-immortalized PSC4	This paper	N/A
Mouse: *Rosa26* KO SV40-immortalized PSC5	This paper	N/A
Mouse: *Erbb2* KO SV40-immortalized PSC5	This paper	Clones: 1.1 F4, 1.1 F10
Experimental models: Organisms/strains		
Mouse: C57BL/6J	Charles River Laboratory	Strain number 632
Mouse: NOD scid gamma (NSG)	Charles River Laboratory	Strain number 614
Oligonucleotides		
Ms sgRNA1.1 *Tgfbr2*: GTCCACAGGACGATATGCAG	This paper	N/A
Ms sgRNA1.2 *Tgfbr2*: GGCCGCTGCATATCGTCCTG	This paper	N/A
Ms sgRNA1.3 *Tgfbr2*: GCCCGACTTGGGAACGTGCGG	This paper	N/A
Ms sgRNA1.1 *Areg*: GAGGGGACTACGACTACTCAG	This paper	N/A
Ms sgRNA2.2 *Areg*: GAGCGCGCCAGCGGTAGCAG	This paper	N/A
Ms sgRNA1.1 *Egfr*: GCCTCATTGCCCTCAACACCG	This paper	N/A
Ms sgRNA1.2 *Egfr*: GGCTTAGGGAACTGCCCATG	This paper	N/A
Ms sgRNA2.1 *Egfr*: GATGTACAACAACTGTGAAG	This paper	N/A
Ms sgRNA3.1 *Egfr*: GAGTAACAGGCTCACCCAACT	This paper	N/A
Ms sgRNA1.1 *Erbb2*: GTTGGGTACCCGCGGCTCCGG	This paper	N/A
Recombinant DNA		
Lenti-Cas9-Blast plasmids	Sanjana et al.[59]	Cat# 52962, Addgene
SV40 large T antigen plasmid	Ohlund et al.[9]	N/A
LRGN (LentisgRNA-EFS-GFP-neo) plasmid	Biffi et al.[3]	N/A
Software and algorithms		
Vevo LAB software program (version 5.7.0)	Visual Sonics	https://www.visualsonics.com/product/software/vevo-lab
ImageJ	Schneider et al.[61]	https://ImageJ.nih.gov/ij/
Aperio ImageScope	Leica Biosystems	N/A

(*Continued on next page*)

Continued

REAGENT or RESOURCE	SOURCE	IDENTIFIER
GSEA program	Broad Institute	https://www.gsea-msigdb.org/gsea/index.jsp
Salmon (v 1.9.0)	Patro et al.[62]	https://combine-lab.github.io/salmon/
Tximport R package	Soneson et al.[63]	https://bioconductor.org/packages/release/bioc/html/tximport.html
DESeq2 R package (v 1.40.2)	Love et al.[64]	https://bioconductor.org/packages/release/bioc/html/DESeq2.html
clusterprofiler R package (v 4.8.2)	Wu et al.[65]	https://bioconductor.org/packages/release/bioc/html/clusterProfiler.html
Morpheus	Broad Institute	https://software.broadinstitute.org/morpheus
"GSVA" method	Hanzelmann et al.[68]	https://bioconductor.org/packages/release/bioc/html/GSVA.html
CellRanger v7.0.1	10X Genomics	https://github.com/10XGenomics/cellranger
CellBender	Fleming et al.[69]	https://github.com/broadinstitute/CellBender
SOLO from scvi-tools	Bernstein et al.[70]	https://github.com/scverse/scvi-tools
Harmony	Korsunsky et al.[71]	https://github.com/immunogenomics/harmony
Scanpy	Wolf et al.[72]	https://github.com/scverse/scanpy
Python implementation of inferCNV of the Trinity CTAT Project		https://github.com/broadinstitute/inferCNV
MAST R package	Finak et al.[74]	https://github.com/RGLab/MAST

RESOURCE AVAILABILITY

Lead contact

Further information and requests for resources and reagents should be directed to and will be fulfilled by the lead contact, Giulia Biffi (Giulia.Biffi@cruk.cam.ac.uk).

Materials availability

All unique/stable reagents generated in this study will be made available from the lead contact with a completed Materials Transfer Agreement.

Data and code availability

(1) All RNA-seq and single-nuclei RNA-seq data generated in this study have been deposited at the GEO and are publicly available as of the date of publication. The GEO Superseries accession number is listed in the key resources table.
(2) This paper does not report original code.
(3) Any additional information required to reanalyze the data reported in this paper is available from the lead contact upon request.

EXPERIMENTAL MODEL DETAILS

Animals

Male and female C57BL/6J (strain number 632) and NSG mice (strain number 614) aged 68 weeks were purchased from the Charles River Laboratory. All animals were housed in accordance with the guidelines of the UK Home Office "Code of Practice for the Housing and Care of Experimental Animals". Animals were kept behind strict barriered housing, which maintained them at a well-defined microbiological health status. This accommodation precludes access by wildlife, including rodent and insect vectors, and is free of infestation with ectoparasites. All animals were health screened every three months according to the FELASA guidelines (FELASA 2002). All animals were fed expanded rodent diet (Labdiet) and filtered water *ad libitum*. Environmental enrichment included nesting material, structures for three-dimensional use of the cage, an area to retreat, and provision of chew blocks. All animal procedures and studies were reviewed by the CRUK-CI AWERB, approved by the UK Home Office and conducted under PPL number PP4778090, in accordance with relevant institutional and national guidelines and regulations.

Cell lines

The majority of murine PSCs (SV40-immortalized PSC4 and PSC5, unknown sex) and PDAC organoid lines (male T6-LOH, female T69A, female T23-LOH) were previously described.[9,48] KPC-derived (C57BL/6J background) male GB-T12-LOH PDAC organoids and C57BL/6J-derived SV40-immortalized male PSC23 were generated as previously described,[9,48,58] although GB-T12-LOH were cultured with Nutlin-3a (SML0580; Sigma-Aldrich) from passage 0 (rather than from a later passage as for other organoids).

Briefly, to establish PSC23, we utilized two and a half pancreata, and a density gradient centrifugation method with Histodenz (D2158; Sigma-Aldrich) and Gey's Balanced Salt Solution (G9779; Sigma-Aldrich). Briefly, to establish GB-T12-LOH organoids, a KPC tumor was digested with collagenase type XI (C9407, Sigma-Aldrich) and dispase (17105-041, Gibco). All PDAC organoids used in this study have been derived from KPC GEMMs and have undergone loss of heterozygosity (LOH) of the *Trp53* WT allele (see Oni and Biffi et al.[48]). SV40-immortalized human PSCs were previously described[3] and primary lines had been purchased from ScienCell (3830, unspecified sex). Mouse PSCs and human PSCs were cultured in DMEM (41966029; Gibco) containing 5% fetal bovine serum (FBS). Mouse pulmonary fibroblasts from C57BL/6J were purchased from ScienCell (M3300-57, unspecified sex), SV40-immortalized and cultured in fibroblast medium basal (SC-2301-B, Caltag Medsystems) with 10% FBS. All cells were cultured for no more than 40 passages at 37°C with 5% CO2. Cell line authentication of murine PSCs (PSC4, PSC5, PSC23) was performed using mouse STR profiling by the CRUK-CI RICS core. Mycoplasma testing of 2D cell lines was performed routinely prior to freezing.

METHOD DETAILS

Mouse studies

Orthotopic transplantation mouse models

Orthotopic injections were conducted as previously described.[3] Briefly, single cells (10,000 cells/mouse) prepared from PDAC organoid cultures (T69A or T6-LOH) were resuspended as a 35 μL suspension of 50% Matrigel in PBS and injected into the pancreas of 8 to 10-week-old mice with or without 10,000 (1:1) *Egfr* or *Areg* WT or KO PSCs.

Analyses in NOD scid gamma mice

Pancreatic tumors in NSG mice were imaged once using the Vevo 2100 Ultrasound at three different orientations with respect to the transducer. Tumor volumes of mice with successful (i.e., non-leaked) orthotopic injections were measured at 2–3 angles using the Vevo LAB software program (version 5.7.0, Visual Sonics). Presence of metastasis and ascites was assessed visually at necropsy for any mice with successful (i.e., non-leaked) orthotopic injections.

Neratinib treatment in C57BL/6J mice

Pancreatic tumors in C57BL/6J mice were imaged prior to enrollment (day −1) and at endpoint (day 14) using the Vevo 2100 Ultrasound at three different orientations with respect to the transducer. Tumor volumes were measured at 1–3 angles using the Vevo LAB software program (version 5.7.0, Visual Sonics). Mice with tumor diameters of 6–8 mm were randomized in either the treatment or vehicle arm, and enrolled 1 day after scanning. Tumor volumes were measured as above, and growth rate was measured by dividing the volume at day 14 for the volume at day −1. The EGFR/ERBB2 inhibitor neratinib (S2150 from Selleckchem for flow cytometry and IHC/*in situ* hybridization (ISH) analyses or HY32721 from MedChem Express for RNA-seq and snRNA-seq studies) was prepared daily as a suspension in 0.1% Tween80, 0.5% hydroxyl propyl methyl cellulose in sterile water. Mice were administered vehicle or 60 mg/kg of Neratinib (ERBBi) for 14 days, once a day (in the AM) via oral gavage.

In vitro cell cultures and treatments

For CM experiments, PDAC organoids were cultured for 3 to 4 days in DMEM with 5% FBS (i.e., control media). For transwell cultures, organoids were plated on top of transwell membranes (82051-572; VWR) with PSCs growing in Matrigel (356231 and 356230; Corning) in 24-well plates in DMEM with 5% FBS. For PDAC organoid/PSC co-cultures, both cell populations were embedded in Matrigel and cultured in DMEM with 5% FBS.

PSCs were treated in Matrigel in 5% FBS DMEM with 20 ng/mL human TGF-β1 (T7039; Sigma-Aldrich), 20 ng/mL murine AREG (315-36; PeproTech), 300 nM EGFR/ERBB2 inhibitor neratinib (S2150; Selleckchem), 1 μM EGFR inhibitor erlotinib (S1023-SEL; Stratech Scientific Ltd) or 2 μM TGFBR1 inhibitor A83-01 (2939; Tocris Bioscience) for as long as specified in the figures and/or figure legends.

CRISPR/Cas9 knockout in pancreatic stellate cells

To knock out *Tgfbr2*, *Erbb2*, *Egfr* and *Areg* in PSCs, lenti-Cas9-Blast plasmids (52962; Addgene)[59] were used. PSCs were infected and selected using 2 μg/mL blasticidin (A11139-03; Thermo Fisher Scientific). Single guide RNAs (sgRNAs) were designed using Benchling and cloned into the LRGN (LentisgRNA-EFS-GFP-neo) plasmid (Vakoc Laboratory, modified from LRG plasmid).[3] PSCs were plated as single clones in 96-well plates in the presence of geneticin (10131035; Thermo Fisher Scientific). Knockout was confirmed by western blot analysis or enzyme-linked immunosorbent assay (ELISA). sgRNAs against the *Rosa26* locus were included to generate control (i.e., WT) PSCs.[60]

Receptor tyrosine kinase assays

Phospho-RTK assays (ARY014; R&D Systems) were performed using 300 μg protein and following the manufacturer's instructions. Quantification was performed using ImageJ.[61]

Western blot analyses

All western blots of PSCs are representative examples and have been repeated with at least two different cell lines (biological replicates). PSCs were harvested in Cell Recovery Solution (354253; Corning) and incubated rotating for 30 min at 4°C. Cells were

pelleted and lysed in 0.1% Triton X-100, 15 mmol/L NaCl, 0.5 mmol/L EDTA, 5 mmol/L Tris, pH 7.5, supplemented with complete, mini protease inhibitors (11836170001; Roche) and a phosphatase inhibitor cocktail (4906837001; Roche). Cells were incubated on ice for 30 min before clarification by centrifugation for 5 min at 1,500 g at 4°C. Standard procedures were used for western blotting. Primary antibodies used were HSP90α (07–2174; Merck Millipore), ACTIN (8456; Cell Signaling Technology), SMAD2 (5339; Cell Signaling Technology), p-SMAD2/SMAD3 (8828; Cell Signaling Technology), TGFBR2 (AF532; R&D Systems), ERBB2 (2165; Cell Signaling Technology), p-ERBB2 (2247; Cell Signaling Technology), EGFR (4267; Cell Signaling Technology), p-EGFR (3777; Cell Signaling Technology), CC3 (9664; Cell Signaling Technology). Proteins were detected using anti-rabbit or anti-goat HRP-conjugated secondary antibodies (Jackson ImmunoResearch).

ELISA assays

For ELISA of media, cultures were grown for 3 to 5 days. Media were collected and assayed using the manufacturers' protocols. ELISA assays were used to detect murine AREG (EMAREG; Thermo Fisher Scientific) and murine TGF-β1 (BMS608-4; Thermo Fisher Scientific).

Proliferation assays

For proliferation assays of PSCs in Matrigel, 5,000 PSCs were plated in 52 μL of 50% Matrigel in PBS on white 96-well plates (136101; Thermo Fisher Scientific) and cultured in 100 μL of media with TGF-β, CM with or without inhibitors, as specified in the figures and/or figure legends. PSC proliferation was followed for 5 to 6 days with CellTiter-Glo (G7572; Promega) with measurements every 24 h. Data were normalized to the first measurement (at 3 h post-plating on day 0).

Immunohistochemical and histological analyses

Standard procedures were used for IHC. Primary antibodies for IHC were p-EGFR (ab40815; Abcam), αSMA (ab5694; Abcam) and SV40 large T antigen (ab16879, Abcam). Detection was performed using ImmPRESS[R] HRP Horse Anti-Rabbit or Anti-Mouse IgG Polymer Detection Kit (Vector Laboratories) as secondary antibodies, and ImmPACT(R) DAB substrate kit (Vector Laboratories). Hematoxylin (H-3404, Vector Laboratories) was used as nuclear counterstain. Hematoxylin and eosin and Masson's trichrome stains were performed according to standard protocols. Brightfield images of tissue slides were obtained with an Axio Vert.A1 (ZEISS). Stained sections were scanned with Aperio ScanScope CS and analyzed using the Aperio ImageScope (Leica Biosystems) Positive Pixel Count algorithm. For Masson's trichrome quantification, the percentage of collagen area was determined by calculating the percentage of blue pixels relative to the entire stained area. To quantify αSMA, p-EGFR and SV40 large T antigen IHC, the percentage of strong positive pixels was calculated relative to the entire tissue section (minus necrotic areas) with the Aperio ImageScope (Leica Biosystems) Positive Pixel Count algorithm.

RNA *in situ hybridization* analyses

RNA *in situ* hybridizations were performed with the RNA Scope colorimetric kit (322360; Advanced Cell Diagnostics) and a murine probe for *Areg* (430501; Advanced Cell Diagnostics), according to the manufacturer's protocol. Briefly, < 3-month-old-cut paraffin embedded sections were used. Slides were baked, deparaffinized and treated with hydrogen peroxide (322330; Advanced Cell Diagnostics). Target retrieval was performed leaving slides in boiling water for 15 min followed by treatment with protease Plus reagent (322330; Advanced Cell Diagnostics) for 30 min. Additionally, the AMP5 amplification step was performed for 1 h. To quantify *Areg* RNA ISH stain, the percentage of positivity was calculated relative to the entire tissue section (minus necrotic areas) using the Aperio ImageScope (Leica Biosystems) Positive Pixel Count algorithm.

Flow cytometry analyses

Tumors were processed as previously described.[3] Briefly, tumors were digested using DNase I (D5025; Sigma-Aldrich), Liberase DL (5466202001; Sigma-Aldrich) and collagenase D (1108882001; Sigma-Aldrich), followed by treatment with ACK lysis buffer (A10492-01; Gibco). Cells were blocked for 15 min on ice with CD16/CD32 Pure 2.4G2 (553142; BD Bioscience). For flow-cytometric analysis of CAFs, endothelial cells, epithelial cells and immune cells, cells were stained for 30 min on ice with anti-mouse CD31-PE/Cy7 (102418; BioLegend), CD45-PerCP/Cy5.5 (103132; BioLegend), CD326 (EpCAM)-AlexaFluor 488 (118210; BioLegend), PDPN-APC/Cy7 (127418; BioLegend), MHCII-BV785 (107645; BioLegend), Ly6C-APC (128015; BioLegend) and CD90-PE (ab24904; Abcam). For flow-cytometric analysis of T cells, cells were stained for 30 min on ice with anti-mouse CD45-PerCP/Cy5.5 (103132; BioLegend), TCR-β-Alexa488 (109215; BioLegend), CD3e-Alexa488 (100321; BioLegend), CD8-APC/Cy7 (100713; BioLegend), CD4-APC (100515; BioLegend). For flow-cytometric analysis of macrophages and neutrophils, cells were stained for 30 min on ice with anti-mouse CD45-PerCP/Cy5.5 (103132; BioLegend), CD11b-PE/Cy7 (101215; BioLegend), Ly6C-Alexa488 (128021; BioLegend – not included in the analyses shown), F4/80-BV785 (123141; BioLegend), MHCII-APC/Cy7 (107627; BioLegend – not included in the analyses shown), CD11c-APC (117309; BioLegend – not included in the analyses shown), Gr1-PE (108407; BioLegend). Cells were resuspended in PBS with DAPI and analyzed on a BD FACSymphony cell analyzer. Flow gating strategies were kept consistent between samples to enable comparison across cohorts.

Flow-sorting of pancreatic ductal adenocarcinoma organoid/pancreatic stellate cell co-cultures

Flow-sorting of PDAC organoid/PSC co-cultures was performed following 3.5 days co-culture in Matrigel in 5% FBS DMEM. Following single cell digestion of co-cultures, cells were stained for 30 min on ice with anti-mouse CD326 (EpCAM)-PE (118205; BioLegend) and PDPN-AlexaFluor 488 (127405; BioLegend). Cells were resuspended in PBS with DAPI and sorted with a BD FACSMelody cell sorter.

Flow-sorting of pancreatic ductal adenocarcinoma tumors

Tumors were processed as described above.[3] Cells were blocked for 15 min on ice with CD16/CD32 Pure 2.4G2 (553142; BD Bioscience).

Flow-sorting of CD90$^+$ and CD90$^-$myCAFs

To flow-sort CD90$^+$ and CD90$^-$ myCAFs from PDAC tumors of orthotopically grafted organoid-derived C57BL/6J mouse models, cells were stained for 30 min on ice with the following antibodies: anti-mouse CD31-PE/Cy7 (102418; BioLegend), CD45-PerCP/Cy5.5 (103132; BioLegend), CD326 (EpCAM)-Alexa Fluor 488 (118210; BioLegend), PDPN-APC/Cy7 (127418; BioLegend), Ly6C-APC (128015; BioLegend), MHCII-BV785 (107645; BioLegend) and CD90-PE (ab24904; Abcam). Cells were resuspended in PBS with DAPI and sorted with a BD FACSAria cell sorter. CD90$^+$ and CD90$^-$ CAFs were sorted as DAPI$^-$CD31$^-$CD45$^-$EpCAM$^-$PDPN$^+$Ly6C$^-$MHCII$^-$ CAFs that were either CD90$^+$ or CD90$^-$, respectively.

Flow-sorting following neratinib treatment

To flow-sort epithelial cells and CAFs from PDAC tumors of Neratinib (ERBBi)- or vehicle-treated C57BL/6J mice, cells were stained for 30 min on ice with the following antibodies: anti-mouse CD31-PerCP/Cy5.5 (102419; BioLegend), CD45-PerCP/Cy5.5 (103132; BioLegend), CD326 (EpCAM)-Alexa Fluor 488 (118210; BioLegend) and PDPN-APC/Cy7 (127418; BioLegend). Cells were resuspended in PBS with DAPI and sorted with a BD FACSAria cell sorter. The epithelial cells were sorted as DAPI$^-$CD31$^-$CD45$^-$EpCAM$^+$ cells, while CAFs were sorted as DAPI$^-$CD31$^-$CD45$^-$EpCAM$^-$PDPN$^+$ cells.

Flow-sorting of co-transplantation models

To flow-sort epithelial cells from PDAC tumors of NSG mice co-injected with *Egfr* WT or *Egfr* KO PSCs and PDAC organoids, cells were stained for 30 min on ice with the following anti-mouse antibodies: CD31-PerCP/Cy 5.5 (102419; BioLegend), CD45-PerCP/Cy 5.5 (103132; BioLegend), CD326 (EpCAM)-Alexa Fluor 647 (118212; BioLegend), and PDPN-APC/Cy7 (127418; BioLegend). The epithelial cells were sorted as DAPI$^-$CD31$^-$CD45$^-$EpCAM$^+$ cells.

Reverse transcription quantitative polymerase chain reaction analyses

RNA (100 ng - 1 μg) was reverse transcribed using TaqMan reverse transcription reagents (N808-0234; Applied Biosystems). qPCR was performed using gene-specific TaqMan probes (Thermo Fisher Scientific) and TaqMan master mix (4440040; Applied Biosystems). Target genes are indicated in the figures and figure legends. Gene expression was normalized to *Hprt*.

RNA-sequencing and single-cell RNA-sequencing analyses

RNA-sequencing of pancreatic stellate cells cultured with transforming growth factor β or conditioned media

Samples were collected in 1 mL of TRIzol Reagent (15596018; Invitrogen). RNA was extracted using the PureLink RNA mini kit (12183018A; Invitrogen). RNA concentration was measured using a Qubit RNA Broad Range kit (Q10210; Thermo Fisher Scientific). RNA quality was assessed on an Agilent TapeStation 4200 using the Agilent RNA ScreenTape kit (5067–5576; Agilent Technologies). mRNA library preparations were performed in the Cancer Research UK Cambridge Institute Genomics Core Facility using 55 μL of 10 ng/mL per sample (RNA integrity number, RIN > 8). Illumina libraries were then sequenced on 1 lane of SP PE50 flowcell on the NovaSeq 6000. These RNA-seq data are available at the Gene Expression Omnibus (GEO) under the accession number GEO: GSE219180. Transcript counts were estimated using Salmon (version 1.4.0) against mouse reference genome GRCm38 (release 102) with default settings. Salmon estimated counts were summarized to gene level using the tximport package in RStudio for use with DESeq2. Protein coding genes with fewer counts than 2^5 were filtered out before differential expression analysis (DEA). DEA was performed using DESeq package (V2) with default parameters in R. Genes with adjusted $p < 0.05$ were selected as significantly changed between conditions. GSEA was performed using the GSEA program (Broad Institute) on the Hallmark gene sets (h.all.v7.4) and the C2 canonical pathway collection (C2.all.v7.4) downloaded from the Molecular Signatures Database (MSigDB). Genes were ranked by their *p* values before submitted to GSEA for analysis.

RNA-sequencing of pancreatic ductal adenocarcinoma organoids

The RNA-seq dataset of murine PDAC organoids derived from the KPC mouse model (n = 21, including primary tumor T and metastatic M organoids) is from Oni and Biffi et al.[48]

RNA-sequencing of pancreatic stellate cell/organoid co-cultures

For RNA-seq of PSCs and PDAC organoids flow-sorted from co-cultures, samples were collected in 1 mL of TRIzol Reagent (15596018; Invitrogen). RNA was extracted using the PureLink RNA mini kit (12183018A; Invitrogen). RNA concentration was measured using either a Qubit RNA Broad Range kit (Q10210; Thermo Fisher Scientific) or a Qubit RNA High Sensitivity kit (Q32852; Thermo Fisher Scientific). RNA quality was assessed on an Agilent TapeStation 4200 using the Agilent RNA ScreenTape kit (5067–5576; Agilent Technologies) or the Agilent High sensitivity RNA ScreenTape kit (5067–5579; Agilent Technologies). mRNA library preparations were performed in the Cancer Research UK Cambridge Institute Genomics Core Facility using 30 μL of 5.7–14.7 ng/μL per sample (RIN > 7.1; total yield between 170 and 440 ng). Illumina libraries were then sequenced on 2 lanes

of SP PE50 flowcell on the NovaSeq 6000. These RNA-seq data are available at the GEO under the accession number GEO: GSE243838. FASTQ files of each sample were processed using the same pipeline. Sequenced raw reads were mapped to the mouse reference genome GRCh39 (mm39) and transcript-level abundances were quantified using quasi-mapping Salmon (v 1.9.0)[62] with gcBias parameters. Then, gene-level abundances were aggregated from transcript-levels using Tximport R package (v 1.28.0)[63]. DEA was done using DESeq2 R package (v 1.40.2)[64] using Wald test. Gene expression was considered significantly differential if FDR < 0.05. GSEA were performed using clusterprofiler R package (v 4.8.2)[65] depending on Msigdb gene signatures.[66,67] Pathways with FDR < 0.25 and NES > 1.5 or NES < −1.5 were considered significantly enriched.

RNA-sequencing of cancer-associated fibroblasts and malignant cells

For RNA-seq of CAFs and epithelial cells flow-sorted from PDAC tumors (either following neratinib (ERBBi) treatment – related to Figures 4 and 7 – or from co-transplantation experiments – related to Figure 7), samples were collected in 1 mL of TRIzol Reagent and RNA was extracted using the RNeasy Micro kit (74004; Qiagen), which is specific for low cell numbers (< 50 K). RNA concentration and RNA quality was measured using the Agilent RNA 6000 Nano kit (5067-1511; Agilent Technologies) or the Agilent RNA 6000 Pico kit (5067-1513; Agilent Technologies) on an Agilent 2100 Bioanalyzer. mRNA library preparations were performed in the Cancer Research UK Cambridge Institute Genomics Core Facility using the NEBNext Single Cell/Low Input RNA Library Prep Kit (New England Biolabs) for Illumina (E6420S) and NEBNext Multiplex Oligos (New England Biolabs) for Illumina (96 Unique Dual Index Primer Pair) (E6440S) according to the protocol's guidelines. For samples with a total yield of < 5 ng 8 μL of RNA were used (RIN > 7.2; RNA yield range between 0.22 and 4.4 ng), while for samples with a total yield of >5 ng 7 μL of RNA were used (RIN > 5.6; RNA yield range between 7.11 and 100 ng). We performed 14 cDNA PCR cycles for samples < 1 ng,11 cDNA PCR cycles for samples < 10 ng, and
8 cDNA PCR cycles for samples between 10 ng and 100 ng. For the final PCR step, we performed 9 PCR cycles for samples < 10 ng and 6 PCR cycles for samples > 10 ng. The samples were run on 1 lane of MiSeq V2 nano to check for the balance. Samples were then sequenced on 2 lanes of an S1 PE50 flowcell on the NovaSeq 6000. These RNA-seq data are available at the GEO under the accession numbers GEO: GSE243888 (*in vivo* flow-sorted malignant cells from co-transplantation mouse models of PDAC – related to Figure 7) and GEO: GSE243889 (*in vivo* flow-sorted malignant cells and CAFs from neratinib- or vehicle-treated mouse models of PDAC – related to Figures 4 and 7).

FASTQ files of each sample were processed using the same pipeline. Sequenced raw reads were mapped to the mouse reference genome GRCh39 (mm39) and transcript-level abundances were quantified using quasi-mapping Salmon (v 1.9.0)[62] with gcBias parameters. Then, gene-level abundances were aggregated from transcript-levels using Tximport R package (v 1.28.0)[63]. DEA was done using DESeq2 R package (v 1.40.2)[64] using Wald test. Gene expression was considered significantly differential if FDR < 0.05. GSEA were performed using clusterprofiler R package (v 4.8.2)[65] depending on Msigdb gene signatures.[66,67] Pathways with FDR < 0.25 and NES > 1.5 or NES < −1.5 were considered significantly enriched.

RNA-sequencing of CD90$^-$and CD90$^+$ myofibroblastic CAFs

For RNA-seq of CD90$^-$ and CD90$^+$ myCAFs flow-sorted from PDAC tumors, samples were collected in 1 mL of TRIzol Reagent and RNA was extracted using the RNeasy Micro kit (74004; Qiagen), which is specific for low cell numbers (< 50 K). RNA concentration and RNA quality was measured using the Agilent RNA 6000 Nano kit (5067-1511; Agilent Technologies) or the Agilent RNA 6000 Pico kit (5067-1513; Agilent Technologies) on an Agilent 2100 Bioanalyzer. mRNA library preparation was performed in the Department of Pathology (University of Cambridge) using the SMART-Seq Stranded Kit (634442; Takara Bio) due to low RIN values for most samples according to the protocol's guidelines. We used 7 μL per samples with a total RNA yield between 0.1 ng and 1.2 ng (RIN between 3.1 and 8.7). We performed 10 cDNA PCR cycles for samples < 0.5 ng and
5 cDNA PCR cycles for samples > 0.6 ng. For the final PCR step, we performed 14 PCR cycles. Samples with a total RNA yield < 0.5 ng were eluted in 12 μL, while samples with a total RNA yield > 0.5 ng were eluted in 18 μL. The samples were run on 1 lane of MiSeq V2 nano to check for the balance. Samples were then sequenced on 2 lanes of an SP PE50 flowcell on the NovaSeq 6000. These RNA-seq data are available at the GEO under the accession number GEO: GSE243828.

Heatmap visualization

Heatmaps were plotted using Morpheus (https://software.broadinstitute.org/morpheus).

Gene set variation analyses

GSVA was performed on normalized gene expression using default parameters and the ''gsva'' method[68] on available datasets from TCGA PAAD (n = 168) and TCGA BRCA (n = 1,100). Prior to this analysis, samples in TCGA PAAD with primary diagnosis defined as ''neuroendocrine carcinoma, NOS'' were excluded. Correlation analyses were performed on z-scores of gene expression values or scaled GSVA scores of selected pathways using customized R scripts. The mCAF signature was obtained from the murine breast cancer scRNA-seq dataset of Bartoschek et al.[29] The human myCAF signature was obtained from the human PDAC dataset of Elyada et al.[6]

Single-cell RNA-sequencing analyses

The scRNA-seq datasets of murine and human PDAC samples are from Elyada et al.[6] CAF signatures were obtained from the murine PDAC scRNA-seq datasets of Elyada et al.,[6] Dominguez et al.[5] (for LRRC15$^+$ CAFs) and McAndrews et al.[14] (for cCAF3 CAFs), as specified in the figures and/or figure legends. LRRC15$^+$ CAF and cCAF3 CAF signatures included genes with LogFC > 0.05 and FDR < 0.05. To generate boxplots from these datasets, the average expression of each pathway was calculated per cell in iCAF or myCAF clusters using the scoring function from Scanpy package.

Single-nuclei RNA-sequencing analyses

Single nuclei isolation

Tumor tissues were collected in cryopreservation buffer (FBS: DMSO: (advanced DMEM/F12 (12635010; Thermo Fisher Scientific); P/S; Glutamine; HEPES) = 50:10:40, v/v/v), snap-frozen in liquid nitrogen and stored at −80°C. For single nuclei isolation, tissues were minced into 1 mm^3 pieces with a scalpel at room temperature. Tissues were then transferred to a Dounce homogenizer (40401; Active Motif) with lysis buffer (i.e., 0.1% IGEPAL (I8896; Sigma-Aldrich) + 10 mM NaCl (59222C; Sigma-Aldrich) + 10 mM Tris-HCl at pH 7.5 (T2194; Sigma-Aldrich) + 3 mM $MgCl_2$ (M1028; Sigma-Aldrich) + 0.2 U/μL RNase inhibitor (N2615; Promega) in nuclease free water (PD092; VWR)). Tissues were sequentially disaggregated using first the loose arm and then the tight arm of the homogenizer (typically 10–15 times per arm), with incubation on ice for 2 min in between. Tissues were incubated on ice for 5 additional minutes prior to filtering through a 40 μm strainer (542040; Greiner) using wash buffer (i.e., 0.2 U/μL RNase Inhibitor in PBS (11593377; Thermo Fisher Scientific)). Nuclei in the filtrate were counted on a LUNA cell counter (LUNA-FL; Logos Biosystems) using AOPI (CS2-0106-5ML; VWR) and PhotonSlides (L12005; Logos Biosystems) prior to centrifugation at 4°C at 500 g for 5 min. The pellet was resuspended with an appropriate amount of wash buffer to have approximately 1 million nuclei/mL, filtered through a 35 μm cell-strainer (352235; Corning), followed by counting of nuclei. For each sample, 35,000 nuclei in 43 μL wash buffer were submitted for snRNA-seq processing with 10X Genomics.

Single-nuclei RNA-sequencing

Single nuclei RNA-seq libraries were prepared in the Cancer Research UK Cambridge Institute Genomics Core Facility using the Chromium Next GEM Single Cell 3′ Kit v3.1 (PN-1000268), the Chromium Next GEM Chip G Single Cell Kit (PN-1000120), the Dual Index Kit TT Set A (PN-1000215), and the Chromium Next GEM Single Cell 3' Reagent Kits v3.1 (Dual Index) user guide (Manual Part CG000315 Rev E; 10X Genomics). Isolated nuclei in wash buffer were loaded into Chromium microfluidic chips with 10X Genomics 3′ v3.1 chemistry to generate single-nuclei gel-bead emulsions using the Chromium controller (10X Genomics) according to the manufacturer's recommendations. RNA from the barcoded nuclei for each sample was reverse-transcribed in a C1000 Touch Thermal cycler (Bio-Rad) and all subsequent steps to generate single-cell libraries were performed according to the manufacturer's protocol with no modifications (with 13 cycles used for cDNA amplification). cDNA quality and quantity were measured the Agilent TapeStation 4200 using the Agilent High Sensitivity 5000 ScreenTape (5067–5588; Agilent Technologies), after which ∼375 ng of material was used for gene expression library preparation. Due to variation in cDNA amount between samples, 10, 12 or 14 cycles were used for sample indexing. Library quality was confirmed with the Agilent TapeStation 4200 using the Agilent High Sensitivity D1000 ScreenTape (5067–5584; Agilent Technologies) to evaluate library sizes and the BMG LABTECH Clariostar Monochromator Microplate Reader with Quant-iT dsDNA Assay Kit for high sensitivity (Q33120; Invitrogen) to evaluate dsDNA quantity. Each sample was normalized to equal molar concentration (10 nM) and pooled with each sample using 10% of the sequencing lane. The pool was sequenced on 1 lane of an S4 flowcell Illumina NovaSeq 6000 with following parameters: 28 bp, read 1; 10 bp, i7 index; 10 bp, i5 index and 90 bp, read 2, aiming for 2B reads.

Data pre-processing

First, demultiplexed FASTQ reads were aligned to the mm10 mouse transcriptome reference to extract the unique molecular identifiers (UMI) and nuclei barcodes by using CellRanger v7.0.1. Then, the "remove-background" function from CellBender[69] was used to remove ambient RNA and other technical artifacts from CellRanger output file "raw_feature_bc_matrix". Depending on the total UMI per nuclei versus barcode curve, the parameters 'expected-cells' and 'total-droplets-included' were determined for each sample. Three different values for false positive rate (fpr) parameters were examined: 0.1, 0.05 and 0.01. Fpr = 0.01 was chosen for downstream analysis. To identify doublets, SOLO from scvi-tools[70] was used.

Dimensionality reduction and clustering

All samples were concatenated into one count object and integrated by using Harmony.[71] We used Scanpy[72] workflow steps to process and clustering the data. UMIs were normalized to 10,000 counts. The top 2,000 highly variable genes were identified, principal component analysis was performed, and k-nearest neighbors' graph (k = 10) was built based on the top 30 PCs. Finally, the Leiden graph clustering method[73] was used to identify distinct cell population clusters. Uniform Manifold Approximation and Projection (UMAP) plots were used to visualize individual nucleus profiles.

Estimating copy number variation

A python implementation of inferCNV of the Trinity CTAT Project (https://github.com/broadinstitute/inferCNV) was used on all integrated samples (n = 8). We used the fibroblast cluster as a reference key and a 250-genes window size. The epithelial cluster was found to have greater copy number alteration score than the fibroblast cluster, which confirmed their malignant cell nature due to their *Trp53* LOH status (see Oni and Biffi et al.[48]).

Gene signature scoring for UMAP

Scores for a gene set of interest for each nucleus profiles were calculated based on the average relative expression by using the "score_genes" tool from Scanpy.

Differential gene expression (DEG) analysis

DEGs shown in Figure 4H were determined with the MAST R package,[74] which was used to define upregulated and downregulated DEGs between ERBBi-treated and vehicle-treated PDAC tumors in each cell type cluster. Genes with FDR < 0.05 were considered significant.

Gene set enrichment analysis

To define DEGs prior to GSEA, we applied the pseudobulk method using DESeq2 R package.[64] Then, the clusterprofiler v4.0 R package[65] and gene signatures from Msigdb were used for GSEA.[66,67]

The snRNA-seq data are available at the GEO under the accession number GEO: GSE244142.

QUANTIFICATION AND STATISTICAL ANALYSIS

GraphPad Prism software, Morpheus software (Broad Institute), customized R scripts and Scanpy Python package[72] were used for graphical representation of data. Statistical analysis was performed using paired or unpaired Student's *t* test, non-parametric Mann-Whitney test or chi-square test. All statistical details of experiments are specified in the figure legends, including the number of technical and biological replicates, and how significance was defined.